IMAGING SYSTEMS FOR MINIMALLY INVASIVE MOLECULAR GUIDED CANCER SURGERIES

BY

MEBIN BABU GEORGE

DISSERTATION

Submitted in partial fulfillment of the requirements
for the degree of Doctor of Philosophy in Electrical and Computer Engineering
in the Graduate College of the
University of Illinois Urbana-Champaign, 2023

Urbana, Illinois

Doctoral Committee:

Professor Viktor Gruev, Chair
Professor Kyekyoon Kim
Professor Shuming Nie
Lecturer Hyungsoo Choi

ABSTRACT

Cancer continues to pose a significant threat to the lives of millions of people worldwide. In addition to causing physical distress to the patients from standard regimen, it also impacts their social life and emotional state due to fear of resurgence, grief, and depression. Early detection is critical for a high five-year survival rate and timely treatment. Among many modalities available today to improve cancer treatment, intraoperative near-infrared molecular imaging used in conjunction with endoscopic surveillance and surgeries is emerging as a promising approach that could enable timely detection of cancer. It combines the benefits of using highly specific tumor targeted probes and enhanced visualization of the surgical site in real-time during surveillance or surgery, potentially improving patient outcomes. Despite the gains provided by this novel multimodal platform, there are several limitations that could impede its effectiveness. These challenges include inter- and intra- tumor heterogeneity which could limit the efficacy of systems optimized to detect a single probe, risk of photobleaching during surgical manipulation of the endoscope that could result in failure to detect cancer, and potential damage to vital structures due to reduced perception of depth from visualizing fluorescence information on 2D-displays. This dissertation proposes addressing these challenges mainly by using two endoscopic systems. The first one features multiple probe imaging using a single-chip imaging sensor to enhance the sensitivity and specificity of cancer detection, while the latter detects a single tracer but exhibits high sensitivity to reduce the risk of probe photobleaching. A third system, which utilizes a holographic display to enhance depth perception during cancer surgery, is also presented.

NOTICE

The chapters in this dissertation are based upon the following published paper; the author of this dissertation was the first author for this paper. Funding information and copyright information has been reproduced in each chapter in compliance with the funding agencies and publishers associated with each paper.

Chapter 2: Ref. [1]

Table of Contents

1 Introduction

Cancer is a prevalent disease that affects approximately 40% of men and women during their lifetime, according to the American Cancer Society. While significant progress has been made in improving cancer treatment, approximately one-fifth of patients with cancer still succumb to the disease [2]. According to the World Health Organization (WHO), cancer is the second leading cause of death globally and is responsible for an estimated 10 million deaths each year [3]. Early detection and complete resection of all cancerous tissue are crucial factors that determine a patient's five-year survival rate. Preoperative imaging instruments such as MRI, PET, and ultrasound, along with regular screenings, are increasing the detection of early-stage cancer. However, there is often a disconnect between preoperative surgical information and intraoperative procedures. Surgeons rely on their sight and touch as primary sensing modalities during surgeries, and their experience becomes critical to the success of the procedure. Incomplete cancer resection remains a common problem in many types of surgical procedures, as small cancerous tissues and margins can easily blend in with healthy tissue. Regrettably, this can lead to poor prognosis for patients, as evidenced by up to 25% of breast cancer patients, 35% of colon cancer patients, and as many as 40% of head and neck cancer patients experiencing incomplete resection [4–7].

With recent developments in miniaturized high-resolution cameras and multimodal optics, endoscopic imaging under white-light illumination has provided a pathway toward minimally invasive surveillance and surgeries to facilitate early detection of cancer, faster patient recovery time, lower tissue trauma, and enhanced visualization of critical tissues and organs compared to open surgeries [8–11]. However, white light endoscopy can limit the detection of flat or deeply seated cancerous lesions due to insufficient morphological differences compared to healthy tissue, which can lead to unfavorable clinical outcomes [12–14]. For instance, patients with lung cancer

undergoing white light endoscopic surgeries have a recurrence rate of 29 % to 88% [9,15,16]. Similar trends have been reported for other types of cancer such as breast, esophageal, sinonasal squamous, and colorectal cancers [17–20].

The integration of near-infrared (NIR) molecular imaging with minimally invasive surgeries (MIS) can overcome these limitations by targeting specific biomarkers of tumors and highlighting the location and extent of primary as well as metastatic tumors. Due to the tissue's low autofluorescence, absorption, and scattering in the NIR spectrum, high target-to-background ratios can be achieved for both superficial and deeply seated tumors [21–24]. Furthermore, the use of NIR molecular imaging can also reduce the risk of injury to critical structures adjacent to cancerous tissues compared to traditional methods that rely on visual perception. [25].

1.1 Challenges that impede NIR molecular imaging in minimally invasive surgeries

Although incorporating NIR molecular imaging in MIS has a great potential in detecting cancer intra-operatively, there are several challenges that need to be addressed in order to maximize its effectiveness. For instance, the inter- and intra-tumor heterogeneity caused by mutation and metastasis of cancer cells limits the detection efficacy of single targeting molecular probes leading to variable patient outcomes [26]. Therefore, using a cocktail of carefully selected and optimized NIR molecular probes targeting different tumor biomarkers can achieve higher tumor detection sensitivity and specificity compared to single tracers [27–32]. The multi-probe approach is the next frontier for molecular guided surgery because of the availability of a plethora of tumor-targeted probes that are either FDA approved or nearing approval from regulatory agencies around the world [27]. However, most FDA-approved NIR imaging instruments, especially the ones focused on endoscopic surgeries, are optimized to detect fluorescence from a single NIR tumor-targeting probe and are not suitable for imaging cocktails of molecular probes. Imaging two NIR probes

requires the use of multiple imaging sensors that can result in endoscopic instruments that are bulky with limited potential for clinical translation.

Another challenge associated with the implementation of fluorescence imaging in endoscopic surgeries is related to the variation in the illumination irradiance during the procedure. Unlike open surgeries where a fixed distance between the illumination optics and the target is maintained to ensure stable irradiance, the working distance between the distal tip of the endoscope and the target being examined can change during surgical manipulation of the endoscope, leading to variations in the irradiance. This can be problematic, as high irradiance could lead to accidental probe photobleaching. Consequently, the probe would exhibit low fluorescence levels, which can compromise tumor detection.

While significant progress in the development of tumor-targeting probes and imaging sensors have enabled the application of NIR molecular imaging in cancer surgeries, the display of the fluorescence information in the operating room continues to pose a significant obstacle. Displaying 3D information from the surgical site on 2D displays leads to the loss of depth information that can result in incorrect clinical decisions during tumor removal. This includes iatrogenic damage or incomplete tumor resection. Furthermore, the use of an external 2D display disrupts the surgical workflow, which can prolong the duration of surgery. In MIS, these challenges are further intensified since the surgical site is not directly accessible. The surgeon has to rely solely on the 2D display screens to locate, navigate, and remove the diseased tissues that are highlighted by fluorescence, which can increase the cognitive effort [33]. Additionally, mismatched Field-Of-View (FOV) between the surgical site presented on the monitor and the natural vision would require the surgeon to constantly adjust visual focus that can lead to increased workload and fatigue.

1.2 Contributions toward implementation of NIR molecular imaging in MIS

The overarching goal of my research is to address each of the previously described challenges that can impede the implementation of NIR molecular imaging in MIS. In this section, I summarize my contributions.

1.2.1 Bioinspired color-near infrared endoscopic imaging system for multiple fluorophore imaging

One of my research contributions involves the design, development, characterization, and application of a bioinspired endoscopic system capable of performing multiple fluorophore imaging while simultaneously capturing color image. This system comprises of a single chip multispectral imaging sensor which is modeled after the visual system of a mantis shrimp [34] along with a highly optimized rigid endoscope which features high transmission across a wide spectral range and minimal chromatic aberrations to enable focusing of color and NIR images on the same imaging plane. The image sensor combines three vertically stacked photodetectors with pixelated spectral filters to make three observations in the NIR spectrum while simultaneously capturing color images. The spectral sensitivity of the image sensor is derived from the distinct spectral response of each of the three photodiodes enabling it to differentiate multiple fluorophores in order to address the challenge associated with tumor heterogeneity. Using this system, it is feasible to use multiple probes targeting different biomarkers to enhance the sensitivity and specificity of cancer detection.

Besides designing the system, I have characterized it using several benchtop tests and evaluated its performance in a preclinical and clinical setting. The results from these tests indicate that the optimized endoscopic system achieves a 60% improvement in NIR spatial resolution when compared to a leading FDA approved endoscope. Furthermore, the system demonstrated ratio-

metric imaging capabilities of two tumor-targeted probes in vials which was validated using a murine breast cancer model. Clinical data gathered from fluorescently tagged lung cancer samples on the operating room's back table demonstrated a high tumor-to-background ratio and consistency with the dye discrimination performed using vial.

1.2.2 Evaluation of pitfalls of NIR molecular imaging in MIS

NIR molecular imaging is emerging as a promising tool for minimally invasive cancer surgeries due to its ability to provide real-time, high-resolution images of anatomical structures while simultaneously highlighting the location of the tumor. However, several pitfalls need to be taken into consideration while employing this imaging modality. On this front, my research contribution involves investigating and demonstrating some of these pitfalls. I firstly assessed how the irradiance experienced by a target under surveillance can fluctuate depending on the working distance from the distal tip of the endoscope. During surgical maneuvering of the endoscope, there is a risk of increased irradiance when the surgeon attempts to enhance the visualization of the site being examined with short working distances. In this context, I also examined the photostability of two probes that are commonly employed for image guided surgery and evaluated the time and concentration dependence of these probes to photobleaching when subjected to high irradiance from the excitation source. Results indicate an alarming increase in irradiance when short working distances were used. Additionally, photobleaching effect of the probes was observed both in vials and in animal study reflected in low fluorescence yield.

1.2.3 Design and preliminary evaluation of a highly sensitive endoscopic system for MIS fluorescence imaging

Although MIS offers several benefits over traditional open surgeries, implementing molecular imaging in MIS can introduce difficulties that are almost non-existent in open surgeries. In the

previous subsection, I highlighted several of these issues, including accidental exposure of the probes to high levels of irradiance during surgical maneuvering of the endoscope that could lead to increased cancer misses. Moreover, the risk can be further amplified by the use of smaller lens diameter in endoscopes, which can adversely affect the sensitivity of fluorescence detection during endoscopic surgeries. This becomes increasingly important when the system attempts to detect weak fluorescence either from low probe aggregation at the targeted site or when the tumor is deeply seated in the tissues. I provide a potential pathway to address some of these challenges by designing an endoscopic system that incorporates a highly sensitive CMOS image sensor and an optimized rigid endoscope. The multispectral image sensor features high NIR quantum efficiency, high dynamic range, and low read-out rates. This, in combination with high transmission of the rigid endoscope, enables the system to detect weak fluorescence. Using benchtop tests, murine lung cancer model, and clinical studies of patients with lung cancer, I have evaluated the system performance for NIR molecular imaging in MIS. The chapter approaches the topic from the viewpoint of lung cancer where there is a strong correlation between survival rate and early detection and treatment of cancer.

1.2.4 Holographic imaging for fluorescence-guided surgery

I addressed the challenges related to the use of 2D displays for image guided surgery by developing a system which integrates the bioinspired image sensor and a holographic display. This display technology projects fluorescent images as holograms on its optical see-through glasses, enabling the surgeons to view the surgical site using natural sight and simultaneously have access to the fluorescently highlighted tumor location. A calibration routine has been developed to ensure co-registration of the augmented data with the natural eyesight which is critical for surgical applications. Additionally, the system is setup to display pre-operative images, allowing for multi-

modal access with minimal head movements during the surgery. The system was evaluated using a series of experiments using 3D-printed phantoms and a murine breast cancer model. Results from the different studies indicate enhanced accuracy and efficiency in detecting and resecting tumors.

1.3 Organization of the dissertation

Chapter 2 presents the bioinspired endoscopic system that can capture both color and NIR fluorescence images from the scene simultaneously. Furthermore, the chapter explains how the system can distinguish multiple probes in different volumetric ratios. The system's optical characteristics and performance are also highlighted using benchtop tests and clinical back table imaging. In chapter 3, several issues that could threaten the implementation of NIR fluorescence imaging in minimally invasive surgeries are addressed. Chapter 4 details an endoscopic system that utilizes a sensitive scientific camera to potentially overcome some of these challenges that are associated with fluorescence imaging during endoscopic surgeries. Again, the results of system evaluation and performance from benchtop tests and clinical back table imaging are presented. Chapter 5 introduces an intraoperative imaging system that utilizes the bioinspired imaging sensor and a holographic display system. The chapter highlights several system features that can tackle the issues related to the use of 2D displays in the operating room. Chapter 6 provides concluding remarks and discussions on the findings and contributions of the research presented in all the preceding chapters.

2 Bioinspired color-near infrared endoscopic imaging system for molecular guided cancer surgery[1] [2]

For the successful treatment of various types of cancer, early detection of solid tumors is of paramount importance [35]. A favorable prognosis can be achieved when localized dysplastic lesions are surgically removed at the earliest onset of the disease. For example, the five-year post-surgical survival rate for patients diagnosed with early-stage breast and lung cancer is >90% and 70-90%, respectively [2,9]. In contrast, a drastic decline in the survival rates has been reported for patients with advanced-stage cancer (29% for breast and 6% for lung). With recent developments in miniaturized high-resolution cameras and multimodal optics, endoscopic imaging using white light illumination have provided a pathway toward minimally invasive surveillance and surgeries to facilitate early detection of cancer, faster patient recovery time, lower tissue trauma, and enhanced visualization of critical tissues and organs compared to open surgeries [8,9]. However, white light endoscopy provides limited detection of flat or deeply seated cancerous lesions due to insufficient morphological differences compared to healthy tissue, which can lead to unfavorable clinical outcome [12–14]. For instance, patients with lung cancer undergoing white light endoscopic surgeries have a recurrence rate of 29% to 88% [9,15,16]. Similar trends have been

[1] The work in Chapter 2 was funded by grants from the U.S. Air Force Office of Scientific Research (FA9550- 18-1-0278), Congressionally Directed Medical Research Programs (W81XWH-19-1-0299), National Science Foundation (2030421), and National Institute of Health (1P01CA254859).

[2] The work in Chapter 2 has been derived from the accepted manuscript for [1] in accordance with Optica's "Copyright Transfer and Open Access Publishing Agreement." The publisher has requested that this material be distributed with the following notice:

Link to Published Version: https://doi.org/10.1117/1.JBO.28.5.056002

reported for other types of cancer such as breast, esophageal, sinonasal squamous, and colorectal cancers [17–20].

The emergence of molecular imaging in MIS has been driven by this inherent limitation with white light endoscopy (WLE). These systems operate in conjunction with fluorescent probes, which target tumor specific biomarkers to highlight the location and extent of primary as well as metastatic tumors. Using the combination of white light and fluorescence imaging, surgical guidance is enhanced as both the anatomical features and the fluorescently highlighted diseased tissues can be simultaneously visualized. Employing a probe that operates in the NIR window is highly preferred since it allows for deep tissue imaging that enables detection of tumors that are not superficial. Furthermore, due to biologic tissue's low autofluorescence, absorption and scattering in the NIR spectrum, a high target to background can be achieved [21,22,24]. Moreover, unlike visible probes, NIR probes enable seamless separation between white light and fluorescence imaging [20,21].

Although cancer detection has greatly improved with the implementation of fluorescence imaging, inter and intra tumor heterogeneity caused by mutation and metastasis of cancer cells limits the detection efficacy of single targeting molecular probes leading to variable patient outcome [26]. Therefore, a cocktail of carefully selected and optimized NIR molecular probes targeting different tumor biomarkers can achieve higher tumor detection sensitivity and specificity compared to single tracers [27–32]. A multi-tracer approach is the next frontier for molecular guided cancer surgery because of the availability of a plethora of tumor-targeted probes that are either FDA approved, such as Pafolacianine for targeting folate receptors [36,37], or nearing approval from regulatory agencies around the world. However, most FDA-approved NIR imaging instruments,

especially the ones focused on endoscopic surgeries, are optimized to detect fluorescence from a single NIR tumor targeting probe and are not suitable for imaging cocktail of molecular probes.

Several research groups have reported multispectral imaging capabilities to display color and a single NIR fluorophore using either multiple cameras with spectra-specific optics or by combining pixelated spectral filters with a single camera [38,39]. The latter approach offers multiple benefits over the former including smaller devices, better ergonomics, and inherent co-registration of NIR and color images. However, the fluorophores used for such an imaging platform must feature an emission spectrum that closely aligns with the transmission spectra of a specific filter from the filter array, thereby imposing restrictions on the probes that can be utilized for fluorescence imaging. In contrast, with the multiple camera approach, this issue can be addressed by tweaking the optics to accommodate different fluorophores. The complexity of the design worsens when multiple probes are to be imaged and differentiated. With the single camera approach, the design of the pixelated filters becomes challenging, as the number of filters with distinct transmission spectra to capture fluorescence from the different probes increases with the number of probes used. This would result in a reduced number of pixels available per probe, ultimately impacting the spatial resolution. Likewise, in the case of multi-camera systems, incorporating a new probe into the system would require additional NIR cameras, leading to difficulties in achieving precise focusing and multimodal co-registration. This would make the approach impractical. For both imaging strategies, differentiation will be impeded if there is an overlap of emission spectra between the different probes due to cross-interference.

Recently, our group reported the development and clinical evaluation of a single-chip hexa-chromatic imaging sensor [34]. The image sensor is modeled after the visual system of the mantis shrimp, combining vertically stacked photodetectors with pixelated spectral filters to make three

observations in the NIR spectrum while simultaneously capturing color images. This approach is radically different from current state-of-the-art multispectral imaging systems which combine multiple cameras and complex optical elements, while still only imaging single molecular tracers. The bioinspired sensor can image at least three NIR fluorophores between 700 nm and 1000 nm because of the unique pixel architecture. Furthermore, this new imaging approach enables differentiation of fluorophores that could be excited using the same excitation source and have emission peaks that are 20 nm apart – a feature that is not featured in any FDA-approved imaging instrument.

Having access to a multispectral imaging platform solves only half of the design problem for multi-probe imaging in MIS systems, as it must be accompanied by an endoscope that is optimized to address several design challenges. Integrating a single camera with the current state-of-the-art rigid endoscopes can be suboptimal, due to chromatic aberrations that could be introduced in the endoscopes. In contrast, with the multicamera approach, chromatic aberrations can be corrected to some extent by independently adjusting the focus of the NIR and color cameras. More recently, conventional endoscopes which utilize fiber optics or lenses are being replaced by endoscopes with a chip on the distal tip to minimize the losses during the light's return path to the detectors. The issues previously described for multi-probe imaging with different approaches would also plague the chip-on-tip approach but with higher severity. For instance, with the multi-camera approach, the endoscope design would be practically infeasible as the number of miniature cameras that must be assembled at the tip of the scope will increase with the number of probes employed.

In this chapter, I will demonstrate an endoscopic imaging system capable of simultaneously imaging and resolving two NIR fluorophores while concurrently capturing color images. The

system uses a custom rigid endoscope and the bioinspired image sensor. I will present the results of the system's optical characterization performed using standard benchtop experiments and compare its performance against a NIR compatible endoscope from Karl-Storz. I will also demonstrate the system's multiple NIR probe imaging and resolving features firstly using a monochromator and then in a 4T1 murine model of breast cancer where two tumor-targeted NIR probes were administered. Furthermore, I will also demonstrate the feasibility of the system for potential clinical translation by showing results from *ex vivo* imaging of human lung cancer specimens collected during fluorescence guided surgery.

2.1 Primary system design requirements

For color and multiple NIR fluorophore imaging, the image sensor and the endoscope must meet several requirements which are detailed in this section.

2.1.1 Camera

To accommodate multiple NIR fluorophore imaging along with white light imaging, it is critical that the camera demonstrate high sensitivity for a wide spectral range from Visible to NIR. Furthermore, for differentiating the fluorophores, it must be capable of resolving the spectral information within the detected fluorescence signals.

Most commercial and research grade instruments employ the Division of Optical Path (DOP) architecture to handle this requirement. However, such an architecture must specify several external components including multiple image sensors to capture different spectral signals, filter set to block excitation sources, and beam splitters along the optical path to guide the detected signals to cameras tuned for corresponding spectral window [21]. Furthermore, with this

architecture, an algorithm must be utilized to co-register the visible and NIR images from different sensors in real time.

Currently, the field is pushing toward a single-chip solution, due to the benefits of reduced size and ease of use. Systems that utilize single cameras with pixelated spectral filters in modified Bayer pattern (RGB-NIR) have reported spectra resolving capabilities by exploiting the distinct spectral response of each of the filters [39]. The fluorophores used, in this setting, must feature emission spectra that closely align with the transmission spectra of different filter channels, thus adding constraints on the fluorophores that can be used. A more versatile single chip platform that does not depend on the pixelated spectral filter characteristics to resolve the fluorophore would be ideal.

2.1.2 Endoscope

Most previously published works implement multi-modal endoscopic imaging by employing multiple image sensor architecture (DOP) [38,40,41]. It offers the flexibility of independent adjustment of different image sensors depending on the focal planes for Visible and NIR-fluorescent images. Most commercially available endoscopes can be effortlessly integrated using this architecture. In contrast, a single chip imaging system would require a lens system that features high quality correction for chromatic aberration. The implications could be far reaching if the focal plane shift between visible and NIR images are unaddressed, as NIR images may be defocused and could ultimately impact the limit of detection negatively.

Furthermore, for color and NIR fluorescence imaging, the endoscope should feature high transmission for a wide spectral range to transfer the signal to the image sensor with minimal attenuation. The endoscope's illumination guides should similarly be able to transmit wideband and handle the optical power needs.

2.2 Design and characterization of multi-modal endoscopic system capable of imaging and differentiating multiple NIR fluorophores.

My primary contribution for this problem involves the design, development, characterization, and application of an endoscopic system capable of both white light and fluorescence imaging. Furthermore, one of the main objectives was to demonstrate the system's multiple fluorophore detection and discrimination feature. In this section, I will provide details of the various system sub-components and present results from several benchtop tests and preclinical and clinical studies.

2.2.1 System components

The endoscopic imaging system (EIS) essentially comprises of a bioinspired camera, a rigid endoscope, a light guide, and multiple light sources. Below, I provide the specifications of each component to address the system requirements.

2.2.1.1 Camera

Recently, our lab developed a single chip bioinspired image sensor (BIS) that emulates the visual system of mantis shrimp [34]. Every pixel comprises three vertically stacked photodetectors overlaid with long-pass (passband greater than 700 nm) and short-pass (passband lesser than 700 nm) pixelated filter set arranged in checkerboard pattern to yield three visible and NIR channels. The pixelated filters enable the separation and simultaneous visualization of the color and NIR fluorescence images. Figure 2.1 depicts the three channels per pixel labeled as Top, Middle, and Bottom and the transmission of the pixelated filter set.

The imaging device is fabricated in silicon, which has a wavelength dependent absorption coefficient. Since the image sensor's absorption coefficient is much higher in the blue spectrum

compared to red and NIR spectra, lower wavelength photons are absorbed dominantly in the top photodiode compared to the middle and bottom photodiode. Hence, the top (bottom) photodiodes have preferential registration of the blue (red) spectrum for the visible pixels. For the NIR pixels, the bottom photodiodes exhibit the highest quantum efficiency due to the high penetration depth of NIR photons in silicon detectors. Even though the quantum efficiency in the NIR spectrum decreases rapidly for the top and middle photodetectors, a total of three distinct measurements are achieved. The quantum efficiency for the three visible and three NIR photodiodes is shown in Figure 2.2, indicating simultaneous imaging capabilities of both color and multiple NIR channels using a single-chip imaging device.

The spectral sensitivity for the image sensor is achieved by leveraging the distinct spectral response of each vertically stacked photodiode in every pixel. The relative variations in the spectral response due to the different quantum efficiencies across the channels would be unique for fluorophores with distinct emission spectra and can be separated using a simple transformation from Red-Green-Blue (RGB) to Hue-Saturation-Value (HSV) space. In contrast to DOP and modified RGB-NIR architectures where external optical components (dichroic mirrors, pixelated spectral filters, etc.) are utilized, this image sensor offers spectral resolution by exploiting the pixel architecture with the vertically stacked photodetectors.

2.2.1.2 Endoscope

A customized laparoscope (OMEC Medical, San Jose, CA, USA) was utilized for the endoscopic system. It contains several cylindrical lenses with multiple optical coatings to minimize both optical losses in the NIR spectrum and chromatic aberrations between 400 and 900 nm wavelength range. This design ensures that both visible and NIR images are focused on the same imaging

plane. The scope specifications are 4mm (10mm) diameter, 30 deg view angle, and 30mm (60mm) length.

2.2.1.3 Light guide

Multiple customized bifurcated fiber bundles were utilized to couple light from the sources to the light post of endoscope. The fiber guides used were optimized for both visible and NIR spectra and rated for high power wattage. The Numerical Aperture (NA) was specified to couple light from the sources with minimal losses.

2.2.1.4 Light sources

For multiple fluorophore imaging platform, 3 different light sources were utilized. UHP-T-WDS-DI (Prizmatix, Israel) was used for white light. To excite the fluorophores, R0785MU6000M4S (Innovative Photonic Solutions, Plainsboro, NJ, USA) and BWF2-665 (B&W TEK, Plainsboro, NJ, USA) were used to excite two probes IR800 and IR680 respectively.

The System setup used for most of the studies is displayed in Figure 2.3. Figure 2.4 displays the spectrum of the white light source.

2.2.2 Optical characterization- spatial resolution

A series of optoelectronics tests were performed with the EIS and compared with an FDA-approved endoscope from Karl Storz. First, I evaluated the effect of chromatic aberrations on the spatial resolution of the EIS and a Karl Storz's endoscope coupled with the single-chip, bioinspired imaging sensor (KS+BIS). Chromatic aberrations are typically introduced by the individual cylindrical lenses in the endoscope and can cause visible and NIR images to be focused on different imaging planes (Figure 2.5). Consequently, if the endoscope is focused on features obtained under

white light illumination (i.e., based on color images), the NIR images could be out of focus leading to reduction in both spatial resolution and NIR sensitivity.

The spatial resolution of the EIS and Karl Storz's endoscope coupled with BIS was evaluated using USAF 1951 resolution target (Edmund Optics, Barrington, NJ, USA). The USAF resolution chart was back-illuminated using an integrating sphere (IS200-4, Newton, NJ, USA) coupled with two light sources: a visible LED and a 785 nm laser light source. The integrating sphere ensures uniform illumination of the target. The endoscope was initially focused under white light (WL) illumination using color images. The working distance for the endoscopes was adjusted depending on the groups targeted on USAF chart (10 mm for groups 1 and 2, and 0.2 mm for groups 4 and 5). Subsequently, the WL was replaced with NIR illumination without readjusting the focus to acquire NIR images. The vertical elements 3 to 6 in group 5 within the USAF target were selected to determine the spatial resolution in terms of line pairs per millimeter (lp/mm).

Figure 2.6-a displays the intensity profile for both color and NIR images across the horizontal lines in group 5. From this figure, we can observe a good correspondence between the NIR and color images captured by the EIS when imaging high-frequency horizontal elements. When high frequency elements in group 5 were imaged, the intensity contrast reduced but were still differentiable. On the contrary, Karl Storz endoscope with BIS exhibited a noticeably lower spatial resolution in the NIR spectrum compared to the visible spectrum. Although the color image remained in focus for elements with high spatial frequency, the NIR image was aliased (i.e. blurred) and could not differentiate high-frequency elements. The intensity profile indicates that the EIS was able to resolve elements that were 9 µm apart (i.e. 57 lp/mm) for both color and NIR images. In contrast, Karl Storz endoscope with BIS demonstrated a spatial resolution of 9 µm under visible illumination but only 15 µm resolution under NIR illumination. This indicates that

the EIS has 60% higher spatial resolution in the NIR spectrum when simultaneously imaging color images compared to Karl Storz endoscope coupled to a single-chip color-NIR camera.

Next, I imaged a depth of focus calibration target to emulate endoscopic imaging scenario where targets with different spatial frequency can appear simultaneously at different distances from the tip of the endoscope. The target was placed at 45 degrees relative to the endoscope's field of view (FOV), targeting the horizontal bars with 15 lp/mm. The white light illumination was utilized to focus the bars at a specific depth within the scope's field of view (FOV). Next, the white light was replaced with 785 nm illumination to acquire NIR images without readjusting the focus. For analysis, the intensities of a row of pixels within the endoscope's FOV was plotted at different depths. The same set of pixels were used for the visible and NIR images. The results from the two endoscopes, under the same testing conditions, were compared to assess each scope's capabilities to address focal plane shift between visible and NIR images. Data was recorded using custom software and analyzed using MATLAB.

Figure 2.6- b shows visible images, NIR images and intensity cross profile for both imaging modalities. It can be observed that the color image registered by both endoscopes can resolve high spatial frequency patterns at different depths. However, the NIR image captured by Karl Storz with BIS is severely aliased, making it difficult to differentiate high spatial frequencies at increasing distance from the tip of the scope. The EIS system was able to spatially resolve these variable frequency targets at different distances due to its higher spatial resolution in the NIR spectrum.

2.2.3 Fluorescence sensitivity

Small molecule tumor targeting probes, such as peptide- or affibody-targeting probes, have fast renal clearance and enable high tumor-to-background imaging within a few hours post administration. This is critical for same day administration of the tumor targeted probes followed

by surgical procedure, which can reduce healthcare cost and avoid hospital infections by minimizing hospital stay.

The system's limit of detection was evaluated for two small molecule tumor targeted probes: 1) an integrin targeted peptide conjugated with IRDye 680RD (IR680-integrin) and 2) an epidermal growth factor targeted affibodies conjugated with IRDye 800CW (IR800-EGF). The limit of detection for indocyanine green (ICG) was also evaluated since it is routinely used for sentinel lymph node mapping and tumor demarcation for various cancer surgeries.

IR680-integrin was prepared by conjugating IRDye 680RD with integrin specific cyclic RGD peptide (cRGDfK, Vivitide, Gardner, MA, USA) as previously reported [42,43]. Briefly, IRDye 680RD-NHS (0.5 mg, LI-COR Bioscience, Lincoln, NE, USA) was dissolved in 0.5 ml phosphate buffer saline (PBS) at pH 7.2 under gentle stirring. Subsequently, the cRGDfK dissolved in 0.5 ml PBS was added to the solution and stirred for 2 hours at room temperature. The cRGDfK-conjugated IRDye 680RD (IR680-integrin) was then purified by dialysis. The concentration of the dye after the conjugation was determined by measuring the absorbance at 680 nm using a UV-Vis spectrophotometer (Genesys 10s UV-Vis Spectrophotometer, Thermo Scientific, Waltham, MA, USA).

For IR800-EGF preparation, EGF-specific affibody (ZEGFR, 0.25 mg, Affibody AB, Solna, Sweden) was initially reduced with Tris (2-carboxyethyl) phosphine (TCEP, Sigma-Aldrich, St. Louis, MO, USA) in 0.5 ml PBS for 30 minutes at room temperature, as previously reported [44]. Afterward, IRDye 800CW-maleimide (0.5 mg, LI-COR Bioscience, Lincoln, NE, USA) dissolved in 0.5 ml PBS was added to the solution and stirred for 2 hours at 40 °C. The ZEGFR-conjugated IRDye 800 (IR800-EGF) was then purified by dialysis. The concentration of the dye after the

conjugation was determined by measuring the absorbance at 775 nm using a UV-Vis spectrophotometer.

The sensitivity of the system was examined by measuring the mean fluorescence intensity (MFI) of IR680-integrin, IR800-EGF, and ICG prepared in serial dilution (0.1 μM to 1 μM) in 2.0 ml vials. Phosphate buffered saline (PBS) was used as a negative control. The limit of detection was determined to be the concentration whereby the MFI of the probe exceeded the MFI of the negative control with 95% confidence. Fluorescence images were acquired under 665 nm laser excitation from IR680-integrin and 785 nm laser excitation from IR800-EGF and ICG, respectively. The total output power of the 665 nm and 785 nm laser was set to 50 and 150 mW/cm2, respectively, with the vial positioned 20 mm away from the distal end of the endoscope. Figure 2.7 displays the mean fluorescence intensity (MFI) recorded with the EIS for the three probes at different concentration levels. Each probe exhibited a linear increase in MFI from 0.1 to 1 μM.

The highest rate of increase was observed with IR680-integrin exhibiting a significantly higher MFI compared to that of ICG at each concentration. This was due to the higher quantum yield of IRDye 680RD compared to ICG along with the sensor's higher quantum efficiency at 700 nm compared to 800 nm wavelength. IR800-EGF and ICG exhibited a similar level of MFI at concentrations > 0.2 μM. However, below 0.2 μM, the MFI of ICG was significantly lower than that of IR800-EGF. Overall, the limit of detection of the EIS was evaluated to be 0.1 μM for all probes with 95% confidence above the background (i.e. PBS, 73.09 ± 0.09).

2.2.4 Spectral resolution

One of the unique features of the EIS is its ability to detect and differentiate multiple NIR spectral bands which has not been featured in any FDA-approved endoscopic imaging systems. The BIS enables NIR spectral imaging because it provides three observations in the NIR spectrum, due to

the vertically stacked photodetectors, each with distinct spectral sensitivities. Although the system provides three channels in the NIR spectrum, it can also image multitude of different NIR fluorophores with distinct spectra just like color imaging where three spectra bands, namely blue, green, and red, can record a scene and differentiate thousands of different colors.

To demonstrate the NIR multispectral imaging capabilities of the EIS, a computer-controlled monochromator (Acton SP2150, Princeton Instruments, Trenton, NJ, USA) was used to generate eight different narrowband illuminations between 680 nm and 820 nm in increments of 20 nm and with full width half maximum of 17 nm (Figure 2.8-a). The intensity for each illumination was matched (231.8±5.0) by adjusting the exposure setting of the image sensor. In other words, the eight spectral bands could not be differentiated based on the intensity recorded. Since the NIR pixels make three observations, each spectral target will produce a different intensity response in the three vertically stacked photodiodes. The raw intensities response from the three photodiodes were transformed to hue-saturation-value (HSV) space, where the spectral content of the targets is represented by the hue and saturation components. Figure 2.8-b depicts the mean confidence intervals in the hue-saturation space for all eight spectral bands. It indicates that the spectral targets between 680 nm and 760 nm were spectrally separable with at least 95% confidence interval or better. The spectral discrimination between 780 nm and 820 nm decreased due to the lower quantum efficiency for the top photodetector in the NIR spectrum.

Next, the EIS was utilized to image various volumetric ratios of two small molecule tumor targeted probes in vials: IR680-integrin and IR800-EGF. IR680-integrin and IR800-EGF were mixed in vials with six different volumetric ratios (ranging from 10:0 to 0:10, 2.0 ml in PBS) and excited simultaneously using 665 nm and 785 nm laser illumination. The hue-saturation response of the detected fluorescence from each mixture was plotted with the 68% and 95% tolerance ellipse. The

three intensity measurements in the NIR spectrum from the vertically stacked photodiodes in the image sensor were converted to the hue-saturation space. It is displayed in Figure 2.8-c. The higher uncertainty in the hue-saturation response from the fluorophore mixtures compared to the narrowband illumination experiments from the monochromator is due to the wider emission spectra of the molecular probes. Furthermore, volumetric ratios where the emission spectrum dominated by IR680-integrin had better differentiation than the ones where IR800-EGF was dominant. This is due to the lower quantum efficiency of the top photodiode at wavelengths above 800 nm, rendering lower signal to noise ratio signals obtained by the top photodiodes in this wavelength spectrum.

2.2.5 Preclinical study

The EIS's ability to detect fluorescence and discriminate multiple NIR fluorophores was evaluated by simultaneously imaging the two tumor-targeted probes in a murine model of breast cancer. Six female immunodeficient mice (J:NU, 2 months old, average weight 25 g; The Jackson Laboratory, Bar Harbor, Maine, USA) was used for the in vivo tumor imaging and ex vivo analysis. Each mouse was inoculated with 4T1 cells (1×10^6 cells per injection) orthotopically into one of the mammary fat pads. The mice were divided into three groups. When the tumor grew to about 1cm in size, the first two groups of mice were administered a 100 µl of 100 µM concentration of either IR680-integrin or IR800-EGF probe while the third group received an administration of an equimolar mixture of the two probes.

The *in vivo* study was conducted to validate the fluorophore-resolving feature observed in the volumetric study. At 6 hours post dye-administration, all mice exhibited strong fluorescence from the tumor regions (Figure 2.9-a).

The fluorescence spectra from the tumors in the three groups of mice were compared by plotting the hue-saturation response recorded with EIS. A good agreement was observed between the hue saturation response from the first two groups of mice where a single probe was administered (Figure 2.9-c) and the corresponding mixtures in the volumetric study in vial (Figure 2.8-c). The hue-saturation response from the third group of mice, where both probes were present, suggests a 30% contribution from IR680-integrin and 70% from IR800-EGF based on the best fit from the volumetric study.

Expression levels of integrin (β3) receptors and epidermal growth factor receptors (EGFRs) in 4T1 cells were assessed by transcript level expression analysis. Initially, RNA-seq reads were downloaded from the GEO database and processed for quality and read length filters using Trimmomatic (v0.38). They were then aligned to the mouse genome (mm10) or Human Genome (hg38) using STAR (v2.7.3). Gene expression levels were quantified across samples using the cuffnorm function in Cufflinks (v2.2.1) and were compared in transcripts per million (TPM) [45–48]. The mean and standard deviation of each gene expression were obtained by averaging 10,000 readings. The RNA transcript analysis of 4T1 tumors indicates similar expression levels for both epidermal growth receptors (EGFRs) and integrin (β3) receptors ($p > 0.05$), which are the target receptor for IR800-EGF and IR680-integrin, respectively (Figure 2.9-b). Hence, initially it was expected that the in vivo results would show about the same level of fluorescence from the two probes at the tumor sites. However, the hue-saturation analysis indicated more dominant fluorescence from IR800-EGF, which could be attributed to many physiological factors including tumor heterogeneity, passive accumulation of the probes, light absorption, and scattering from the skin of the mouse.

To validate the individual contribution of fluorescence from the two fluorophores, each tumor was resected after euthanizing the mice and imaged using the in vivo imaging system (IVIS, Perkin Elmer) with two different excitation sources (675 and 740 nm). Figure 2.10-a shows the emission spectra of tumors treated with the individual fluorophores and the 1:1 mixture. The tumors with IR680-integrin exhibited a strong emission peak at 720 nm and the emission gradually decreased with increasing wavelength. No noticeable emission was detected beyond 800 nm. On the contrary, the tumors with IR800-EGF exhibited emission dominantly at wavelengths beyond 780 nm. When the emission spectra of the tumors from mice administered with the mixture were overlayed on top of the spectra of the individual fluorophores, it closely corresponded to the spectral pattern observed with IR800-EGF. The composite image acquired by the IVIS showed the presence of both fluorophores within the tumor indicated by the red and blue color (Figure 2.10-b), which was consistent with the in vivo analysis.

2.2.6 Clinical study

Six patients diagnosed with non-small lung cancer and undergoing surgical treatment were recruited for an IRB-approved study at the hospital of the University of Pennsylvania. The patients were intravenously administered 0.32 mg/kg of cathepsin-activated ICG probe (VGT-309 - Vergent Bioscience, Minneapolis, MN) at 24 hours prior to surgery which is a cathepsin-binding ICG agent that could selectively activate fluorescence signal in the tumor microenvironment with upregulation of cathepsin [49]. During the surgery, the surgeon performed a wedge resection to remove cancerous nodules that were fluorescently identified using a NIR intraoperative imaging system (Vison Sense, Philadelphia, PA). Immediately after the wedge resection, the nodules were imaged using the EIS on the back table. Figure 2-11-a shows the imaging setup of the EIS for

back-table imaging of lung cancer nodules in the operating room. 785nm laser was used to excite the dye.

Figure 2-11-b shows representative intraoperative visible and NIR fluorescence images of the malignant nodules. High-intensity fluorescence was detected from tumors during the surgery that correlates well with back table images (Figure 2-11-c), while no significant fluorescence was detected from the adjacent normal tissues. EIS was able to differentiate the malignant nodules from the background based on the fluorescence with a 95% tolerance level (Figure 2-11-d), thereby providing high contrast between the tumor and background with a mean TBR of 4.73±0.44. All six tumor regions from the six specimens exhibited significantly higher fluorescence compared to the background. Figure 2-11-e displays the hue-saturation response of the fluorescence signal from the nodules which corresponds to the response from ICG in a vial. The H&E (Figure 2-11-f) and fluorescence images (Figure 2-11-g) of the tumor nodule and normal lobe validate that high-intensity fluorescence was associated with the presence of malignant cells.

2.3 Conclusion

In this chapter, I have emphasized the need for a multimodal endoscopic system capable of imaging and discriminating multiple NIR fluorophores to enhance the sensitivity and specificity of cancer detection. I presented how several research groups have proposed designs to achieve this along with challenges of each of the approaches. I introduced an endoscopic imaging system which incorporates a bioinspired imaging sensor which features multispectral imaging and multi-probe differentiation and an endoscope that is optimized to transmit wide spectra (visible and NIR) with minimal attenuation and chromatic aberrations. Following this, I presented several system characterizations results where I demonstrated high NIR sensitivity, spatial and spectral resolution using benchtop experiments. Finally, I demonstrated the feasibility of the system for clinical

translation with preclinical animal studies and back table imaging of lung cancers nodules resected from human patients demonstrating several features of the system.

2.4 Figures

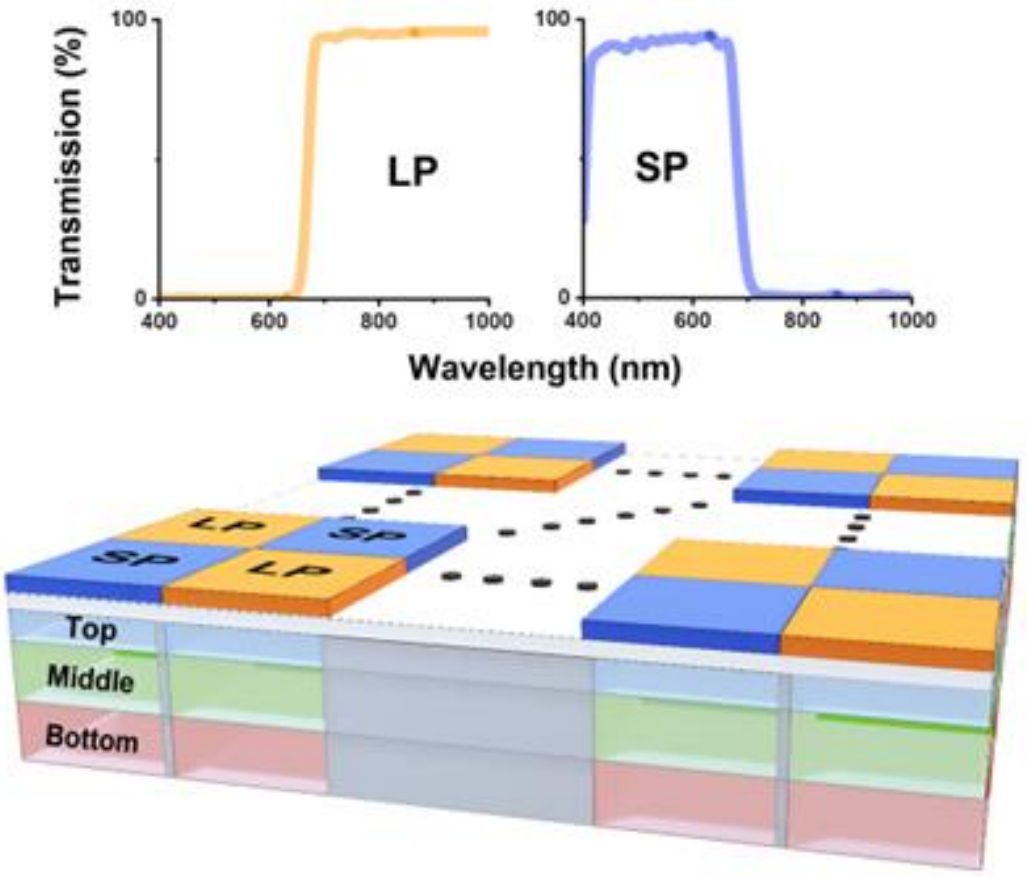

Figure 2.1- The imaging sensor combines an array of vertically stacked photodiodes and pixelated spectral filters to sense six spectral bands.

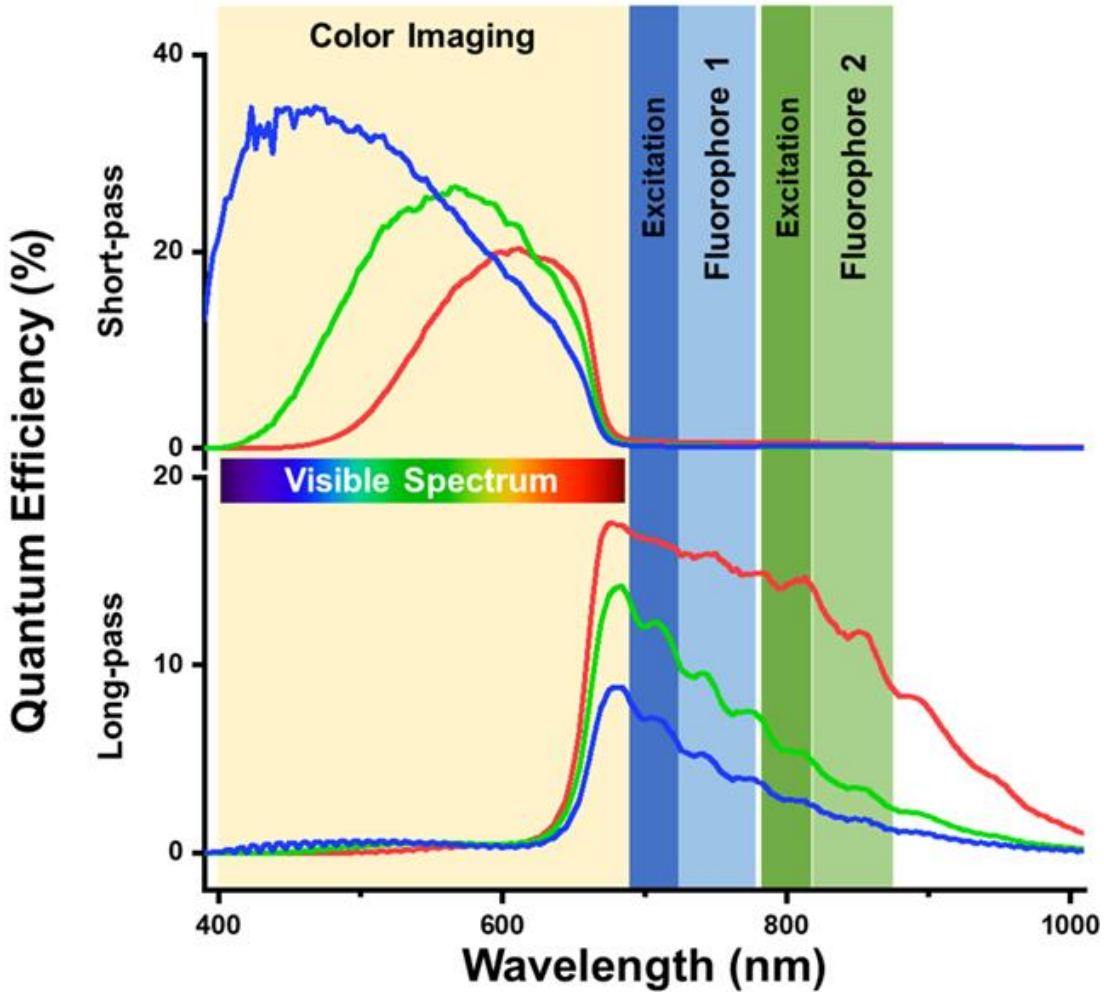

Figure 2.2- The quantum efficiency for the top, middle and bottom photodiode under the long-pass and short-pass pixelated spectral filters.

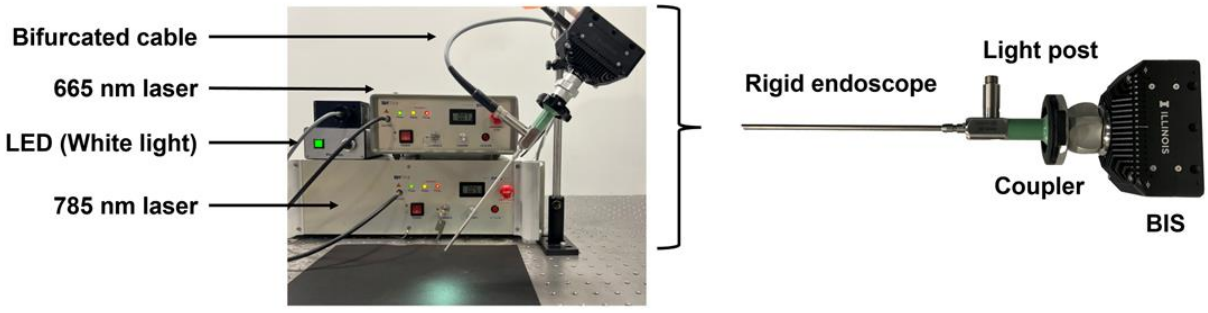

Figure 2.3-A snapshot of the bioinspired endoscopic imaging system for imaging multiple tumor-targeted NIR probes. The system is comprised of a custom-designed rigid endoscope, fiber optical illumination bundle, 665 nm laser, 785 nm laser and the Bioinspired imaging sensor

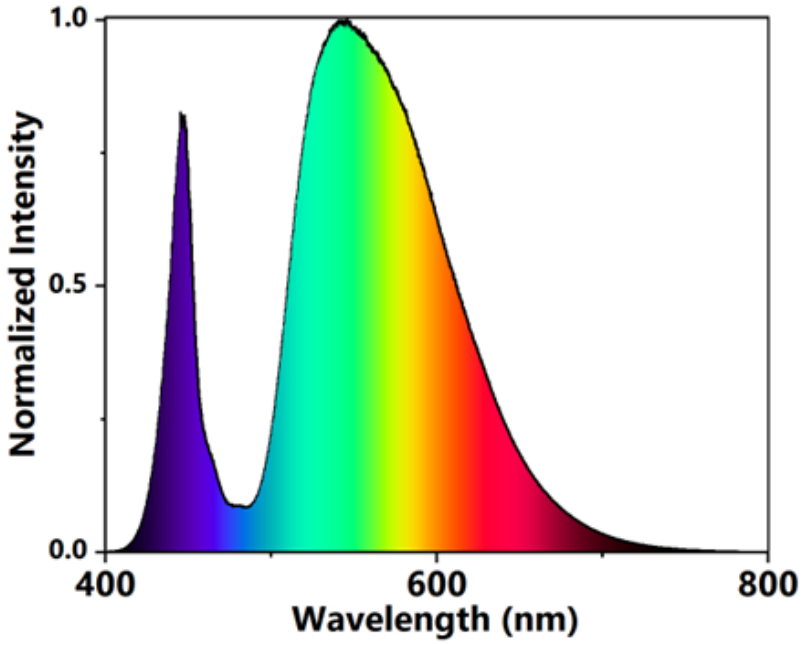

Figure 2.4- Spectrum of white light source used for several imaging studies.

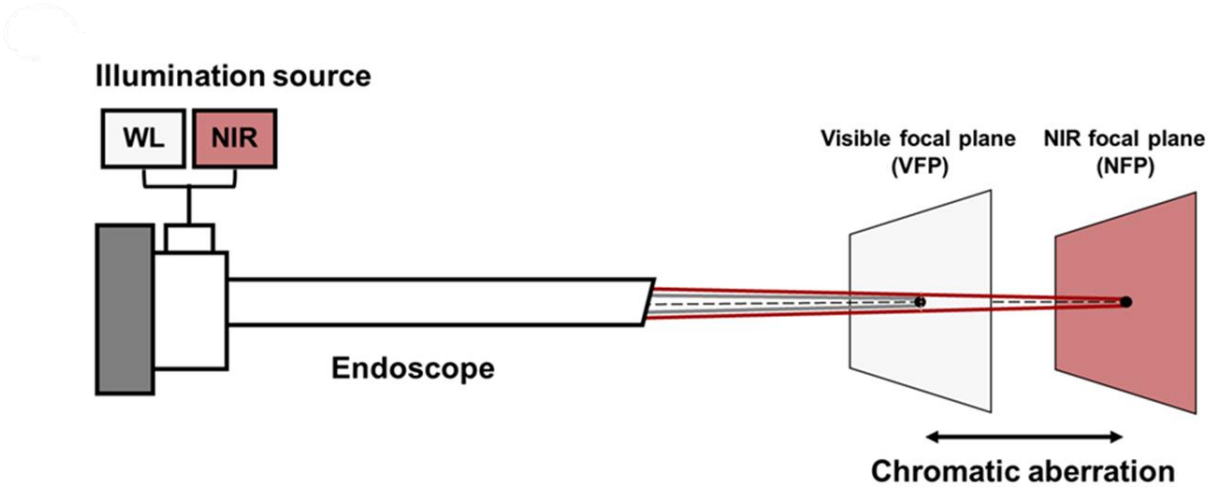

Figure 2.5- Chromatic aberrations in endoscopes lead to different imaging planes when illuminated with visible or NIR light.

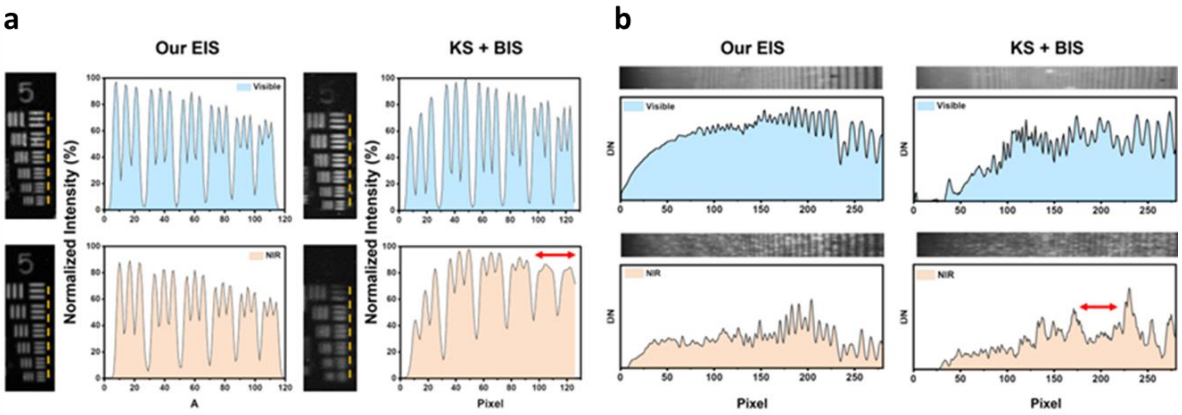

Figure 2.6- a) Visible (top) and NIR images (bottom) of the USAF resolution chart. The resolution of the 6 elements in group 5 (yellow dotted line) was analyzed and plotted as pixel position vs. intensity. (b) Images of an ROI in the slanted depth of focus target under visible and NIR illumination. The corresponding line profiles are plotted below. Red arrows indicate regions where the images in the NIR spectrum are aliased (i.e. blurred).

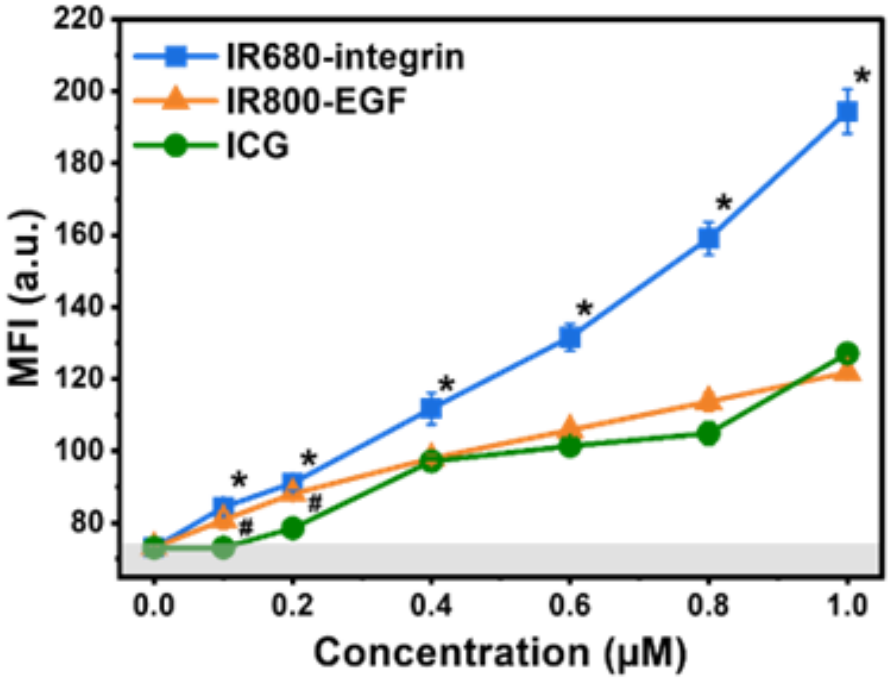

*Figure 2.7- The sensitivity of EIS was analyzed using IR680-integrin, IR800-EGF, and ICG at varying concentrations (n=3). The gray area represents the background signal from a vial with PBS (95% confidence interval). * and # denote the significance difference in MFI of IR680-integrin and IR800-EGF, respectively, with ICG ($p < 0.05$).*

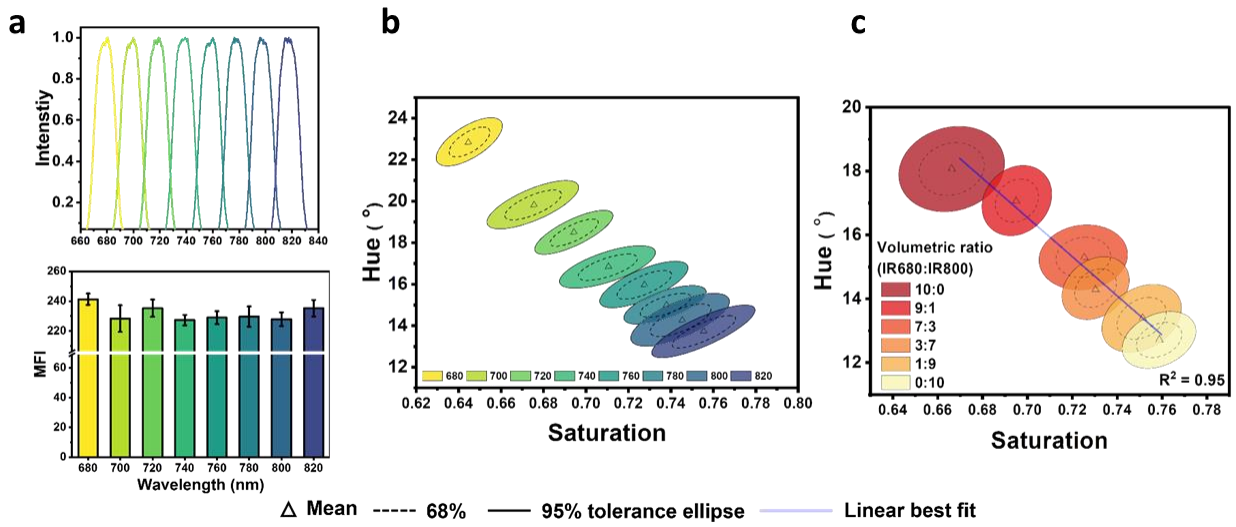

Figure 2.8-(a) The EIS system was illuminated with 8 different narrow-band lights generated from a monochromator. The MFI of these targets had no statistically significant difference (n=3, $p < 0.05$). (b) EIS can spectrally discriminate these eight narrow-band targets despite their similar intensity profiles. The spectral response of EIS is represented by converting the raw intensity data from the three vertically stacked photodiodes into hue-saturation values. (c) Spectral discrimination capabilities of EIS when imaging different volumetric ratios of IR680-integrin and IR800-EGF. Each cluster represents the mean distribution with 68 % and 95% tolerance ellipses. Linear regression was applied to generate a best fit line within the clusters.

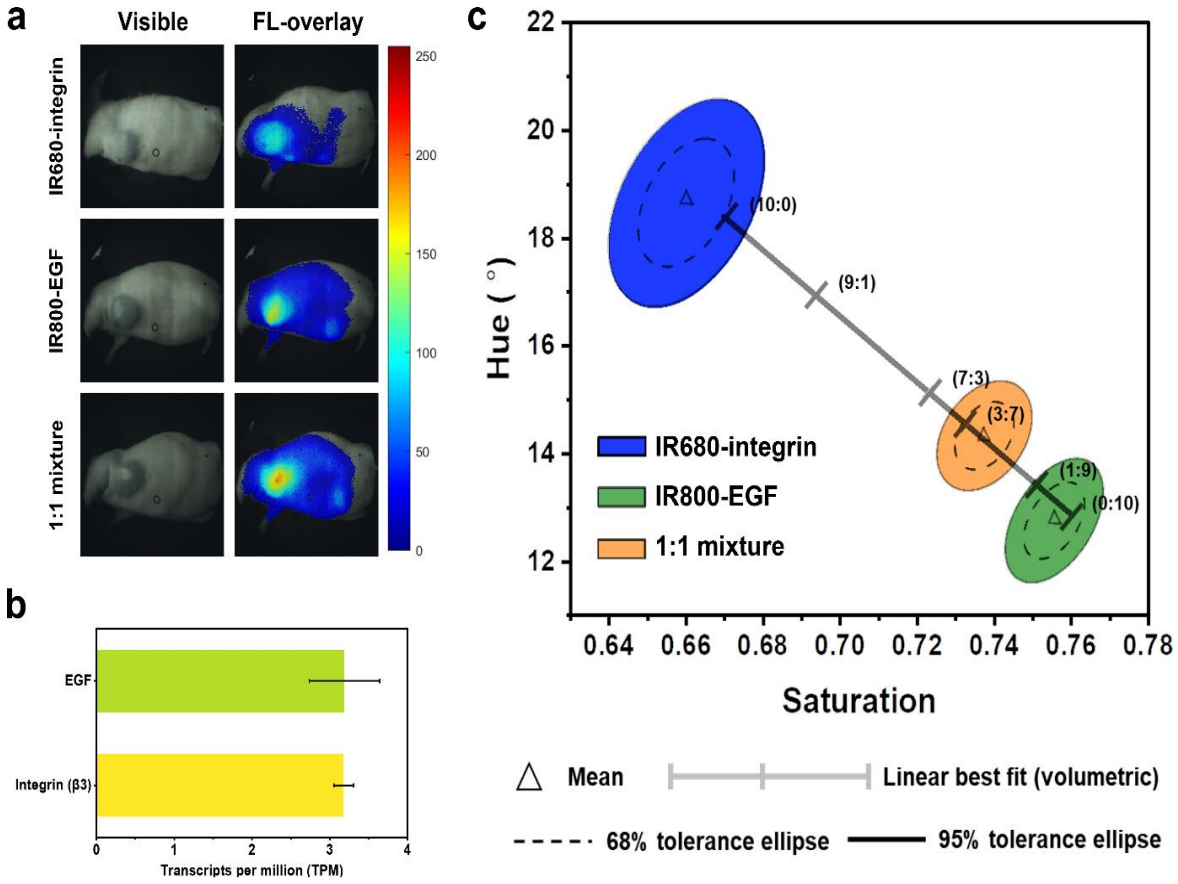

Figure 2.9- In vivo validation of EIS. (a) Visible and fluorescence-overlayed (FL-overlay) images of 4T1 tumor-bearing mice at 6 hours post-administration of IR680-integrin, IR800-EGF, or 1:1 Mixture of the two probes. (b) RNA transcripts of 4T1 tumors showing the expression level of EGFR and integrin receptor β3. (c) Spectral discrimination of the two probes in vivo using EIS. The ratio of the mixed probes at the tumors was estimated by applying the best fit line from the vial study. Each tick represents the mean hue-saturation response of corresponding volumetric ratios of the two fluorophores.

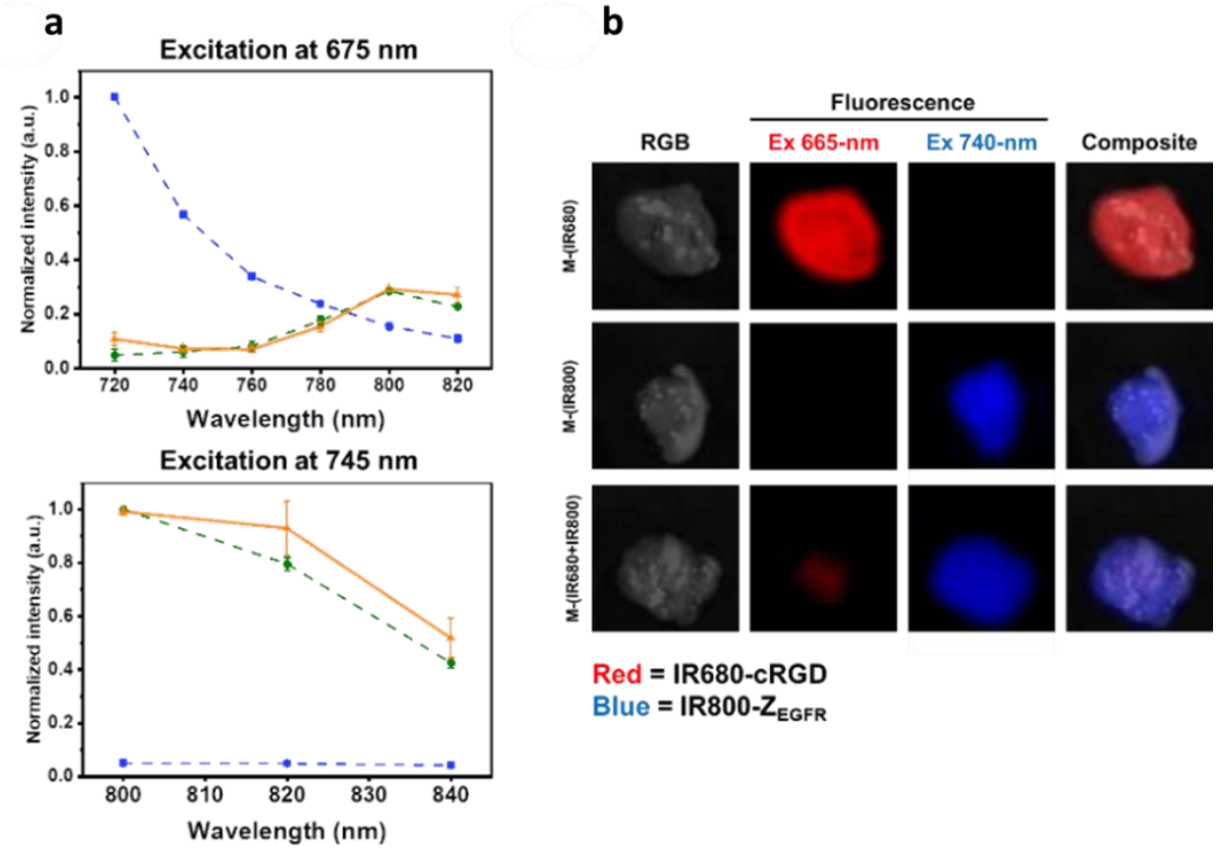

Figure 2.10-(a) The emission spectra and (b) collection of visible and NIR fluorescence images of M-(IR680), M-(IR800), and M-(IR680+IR800) when excited using 685 and 740-nm light sources using the IVIS.

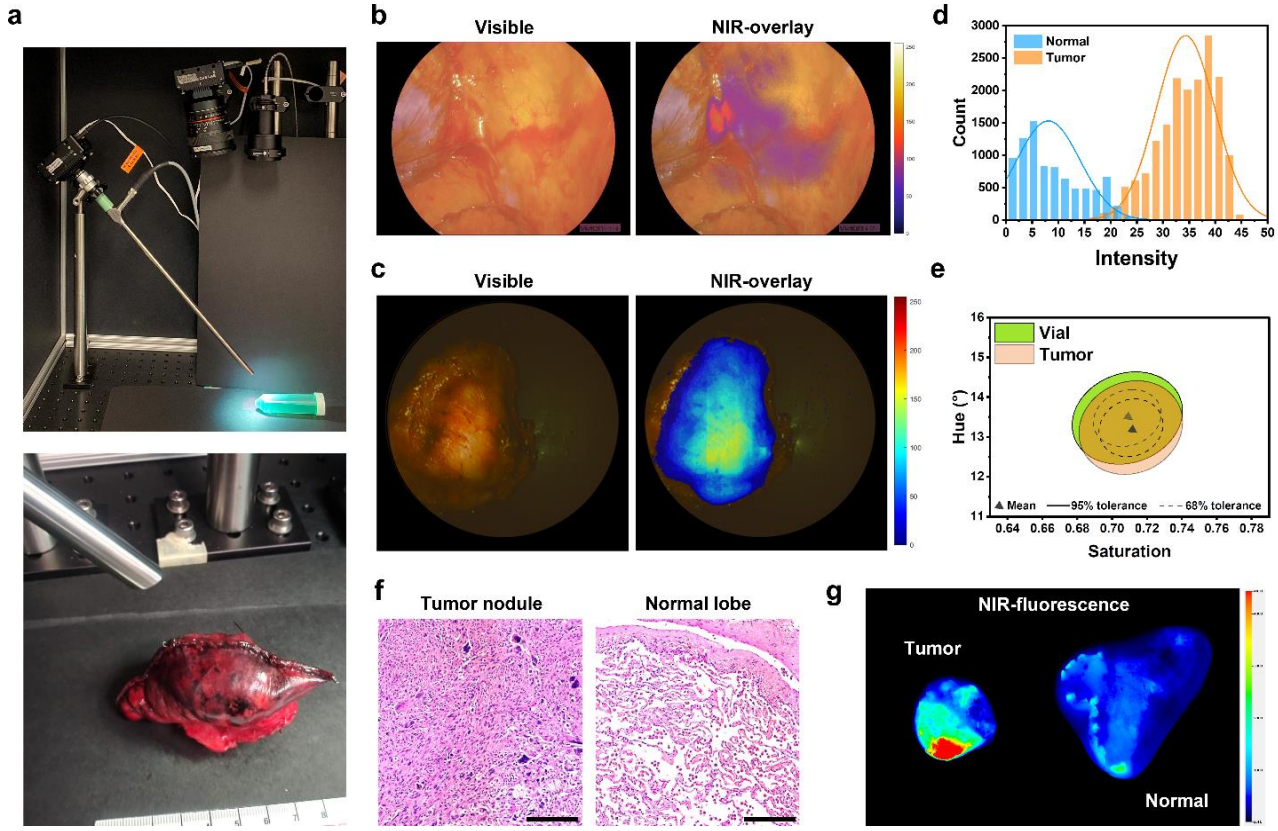

Figure 2.11- Clinical validation of EIS by imaging fluorescently labeled lung cancer nodules on a back table in the operating room. (a) Experimental setup of EIS for the back-table imaging of the resected lung nodules and lobes. (b) Visible and fluorescent images of lung cancer nodules acquired during the operation with NIR Intraoperative imaging system (c) and back-table imaging with EIS immediately after resection. (d) A histogram showing the distribution of fluorescence intensity of the regions of interest marked at the malignant nodules and normal tissue. (e) Hue-saturation response of fluorescence signal detected in the tumor compared to the signal in a vial. (f) Representative H&E images of a malignant nodule and normal tissue. Scale bar: 200 μm. (g) Fluorescence images of the resected tumor nodule and adjacent normal lobe acquired by a NIR scanner.

3 Pitfalls to be addressed for successful translation of molecular fluorescence endoscopy for minimally invasive cancer surgeries.

Minimally invasive surgeries are currently being investigated and implemented for various oncologic applications due to several benefits they offer compared to open surgeries, including early detection of cancer, reduced anesthesia and hospitalization time, faster patient recovery time, lower tissue trauma from minimal incisions, and enhanced visualization of critical tissues and organs [8,9]. However, detecting tumors using white light endoscopy, which is the current standard-of-care for detection of several types of cancer, is severely impeded when tumors are either buried deep under tissue surface or have low differentiation from surrounding healthy tissues [12–14]. Moreover, the lack of haptic feedback during endoscopic procedures poses additional challenges as surgeons must rely solely on visual cues provided by images generated under white light illumination to make clinical decisions [50,51]. This deficiency impairs the surgeon's ability to sense tissue stiffness, which is critical for identifying cancer. These deficits with white light endoscopy could account for unacceptably high local recurrences observed in patients with lung, breast, esophageal, sinonasal squamous, and colorectal cancers [9,15–20].

Endoscopic surgeries implementing molecular imaging using NIR probes could potentially address several of these challenges associated with white light endoscopy. It is emerging as the next frontier for cancer removal surgeries, as it can highlight diseases that may otherwise remain indistinct from its surroundings [52–58]. Additionally, due to the low absorption and scattering of NIR light in biologic tissues, detecting deep-seated cancerous lesions becomes feasible [21,59]. Furthermore, advances in the development of tumor-targeting probes have greatly improved the sensitivity and specificity of cancer detection, particularly in minimally invasive surgeries where visual cues and haptic feedback are limited [27]. Several of these probes have been cleared for

fluorescence guided surgery (FGS) by the FDA and several other regulating agencies around the world. Currently, some of the probes that operates in the NIR window and are being tested in several clinical trials include ICG, Pafolacianine and IRDye800CW-Conjugates [60].

Although incorporating fluorescence imaging in MIS has a great prospect for cancer treatment, there has not been adequate evaluation of some of the factors that could limit its effectiveness. For instance, illumination of target using the excitation light source is a critical requirement for fluorescence imaging. However, unlike open surgeries where the irradiance is stabilized by maintaining a fixed distance between the illumination optics and the target, the use of endoscope for fluorescence-based cancer detection could result in probe photobleaching. The dye that has been aggregated at the target could unintentionally be exposed to high levels of excitation irradiance while the surgeon attempts to locate fluorescently highlighted diseased tissues at different working distances from the surgical site. Consequently, the photobleached fluorescent probe would demonstrate reduced to negligible fluorescence signal and thereby compromise tumor identification. Therefore, the risk of photobleaching of dyes in the context of MIS needs to be thoroughly investigated.

In this chapter, I will firstly present the experimental setup used to investigate some of these pitfalls. Next, I will evaluate the fluctuations in irradiance experienced by a sample placed at different working distances from the endoscope. This is followed by an assessment of the photostability of a few NIR probes that are commonly employed in FGS when exposed to increase levels of illumination irradiance over time and at different concentrations. I will conclude this chapter by demonstrating photobleaching of ICG using an *ex vivo* specimen of a murine lung cancer model.

3.1 System setup

The endoscopic imaging system (EIS) used for the study is displayed in Figure 3.1-a. It consists of the bioinspired imaging sensor (BIS), a 10mm 30 deg. rigid endoscope (OMEC Medical, San Jose, CA, USA) and custom fiber cables (Sunoptic Technologies LLC, Jacksonville, FL, USA) to couple the excitation light from a 785 nm laser (R0785MU6000M4S, Innovative Photonic Solutions, Plainsboro, NJ, USA) into the endoscope's light post. A notch filter with optical density > 6 was used to suppress the excitation light source (NF03-785E, Semrock) which is placed within the camera housing.

Figure 3.1-b illustrates a few system features. It displays the BIS which features three vertically stacked photodiodes per pixel overlaid with alternate long pass (passband >700nm) and short pass (passband >700nm) pixelated spectral filters in checkerboard pattern, enabling the sensor to make three observations in the NIR spectrum while simultaneously capturing visible (color) images.

3.2 Illumination irradiance at different working distances

High numerical aperture is a desired feature for the illumination fibers embedded within the endoscope to ensure that the entire region within the endoscope's field of view (FOV) is lit by the excitation source. However, the resulting diverging beams invariably cause fluctuations in the irradiance at different distances from the endoscope's distal tip. Consequently, a shorter working distance can significantly increase the irradiance in comparison to a longer working distance.

To evaluate the irradiance fluctuations, I initially set the excitation source irradiance to a nominal value of 20mW/cm^2 measured by the optical power meter (PM100D w/ S130VC sensor, Thorlabs) positioned 10cm away from the endoscope's distal tip. Subsequently, I logged the irradiance in

2.5cm decrements of the working distance. Figure 3.2 displays the increase in irradiance with reduced working distances. It peaked at 2.5cm to nearly ~115mW/cm^2.

3.3 Photostability of NIR fluorophores at high irradiance

One of the benefits of endoscopic imaging is its ability to provide detailed visualization of tissue features at short working distances. However, when operated in conjunction with fluorescence imaging, the risk of unintentional photobleaching of administered dyes increases during surgical maneuvering of the endoscope. Due to the potential exposure of fluorophores to high irradiance from the excitation source during endoscopic procedure as demonstrated in the previous test, I examined the fluorescence yield from ICG and IRDye subjected to a high excitation irradiance. The probes were prepared in different concentrations (10μM to 0.1μM) in vials and placed within the endoscope's field of view. The excitation light source was set to an irradiance of 100mW/cm^2.

Figures 3.11-a and 3.11-b display the drop in fluorescence yield versus elapsed time under continual exposure to the excitation source for different concentrations of ICG and IRDye respectively. For similar concentrations, IRDye exhibited superior photostability in comparison to ICG. For instance, for 10μM concentration, negligible fluorescence was measured for ICG after 12 minutes of illumination while IRDye demonstrated detectable fluorescence even after 40 minutes of exposure. Additionally, a strong correlation was observed between fluorescence deterioration and the dye concentration suggesting the need for a careful reassessment of optimal concentration for endoscopic molecular guided surgeries without raising any concern for cytotoxicity.

3.4 A549 ex vivo imaging.

I also examined the impact of photobleaching *in vivo* in murine lung cancer model. One female immunodeficient mouse (J:NU, 2 months old, average weight 25 g; The Jackson Laboratory, Bar Harbor, Maine, USA) was inoculated with A549 cells (1×10^6 cells per injection) into one of the mammary fat pads. When the tumors grew to about $1cm^3$ in size, the mouse was intravenously administered with 2.5mg/Kg concentration of ICG. After 6-hour post-administration, the mouse was sacrificed. The tumor was harvested for *ex vivo* imaging using the imaging system under high laser irradiance ($100mW/cm^2$) at 130 ms exposure setting to monitor the degradation of fluorescence signal due to photobleaching. Data was recorded for several seconds in one-minute increments and analyzed using matlab scripts. Regions of interest were selected from tumor, healthy tissue, and the background to determine the fluorescence intensity over time. Figure 3.4 displays the detected fluorescence intensity trend from the three regions. The fluorescence signal from the tumor degraded over time, while the signal from the healthy tissues and the background remained stable for the entire duration of exposure to excitation light. Based on the trend in intensity drop, the concentration in tumor closely correlates with 200nM concentration.

The manufacturer recommended dosage for ICG administration is 320μM for mice while that for dyes like IRDye800-RGD is much lower at around 10μM due to its targeting characteristics, resulting in much lower dye concentration at the tumor site with lower photostability. Therefore, criterion used for optimal dosage based on open surgeries should not be enforced for endoscopic fluorescence imaging. Instead, a careful evaluation of dosage for different fluorophores in the context of endoscopic imaging is appropriate.

3.5 Conclusion

In this chapter, I have highlighted some of the challenges associated with the use of NIR fluorescence imaging in minimally invasive surgeries that, if not addressed in a timely manner, could limit its effectiveness. I demonstrated how the fluctuation of irradiance at the surgical site during the surgical maneuvering of the endoscope could lead to photobleaching of the probes. This could pose a big threat to the patient during intra-operative surgery due to potential failure in identifying cancer. I also demonstrated photobleaching of two commonly used probes using both vial studies and *ex vivo* imaging of murine lung cancer model.

3.6 Figures

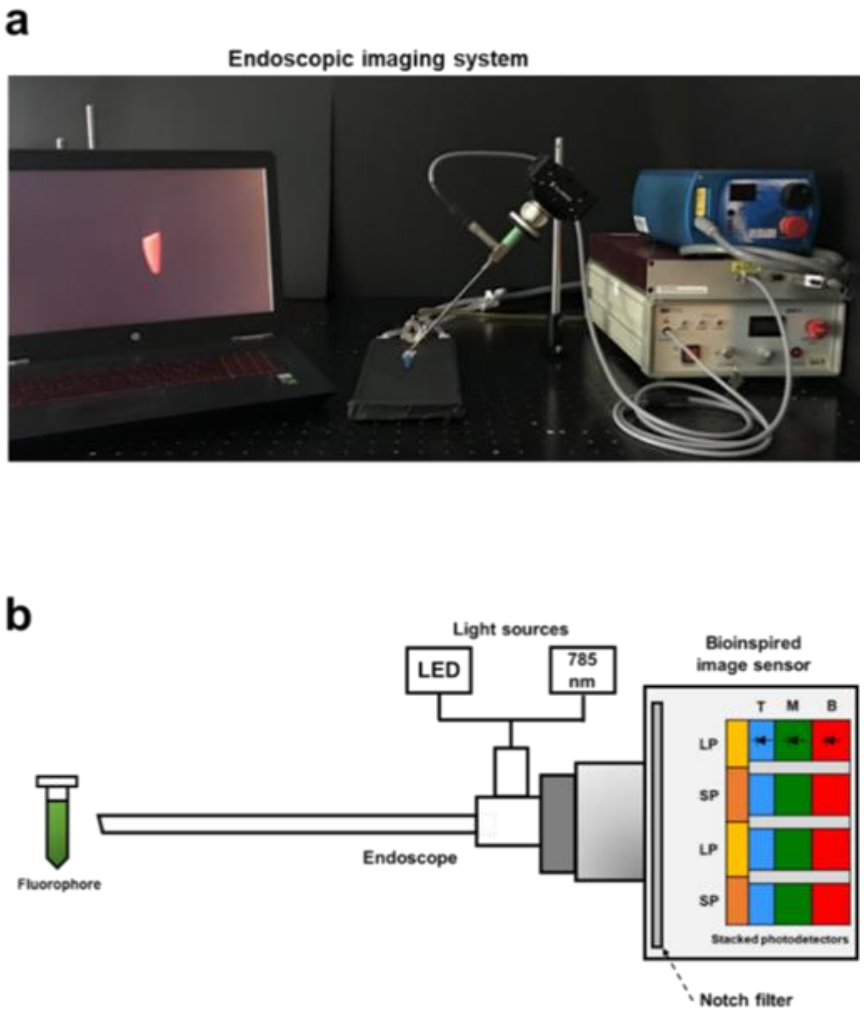

Figure 3.1- Experimental setup and schematic illustration of the endoscopic molecular imaging system with the bioinspired image sensor and HoloLens. (A) The imaging setup with the light sources, the image sensor, and the endoscope. (B) Schematic illustration of the vertically stacked image sensor with the pixelated spectral filters which allows for making three observations in Nir while simultaneously capturing visible image. White Light and Nir excitation light are coupled into the endoscope using bifurcated bundles.

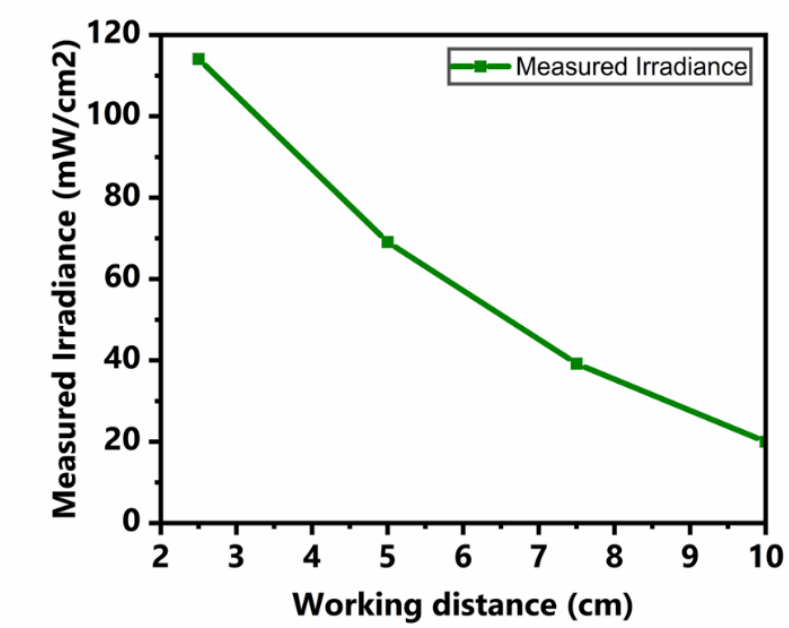

Figure 3.2- The irradiance measured at different working distances from the endoscope using an optical power meter.

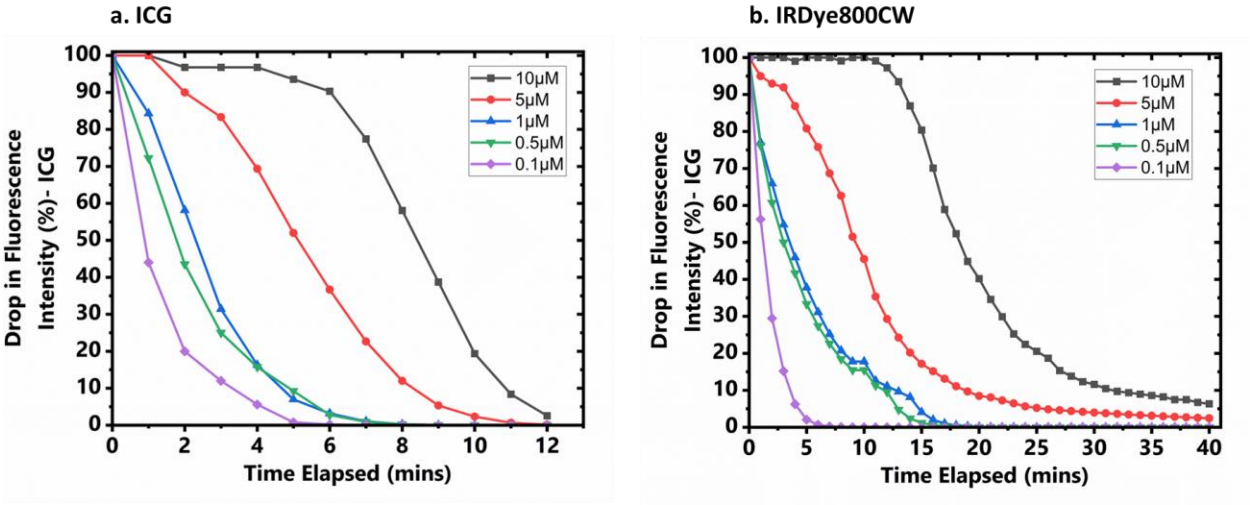

Figure 3.3- Percentage drop in fluorescence intensity detected by the endoscopic system under continual exposure of 100mW/cm2 irradiance for fluorophores a. ICG and b. IRDye, prepared in vials in different concentrations.

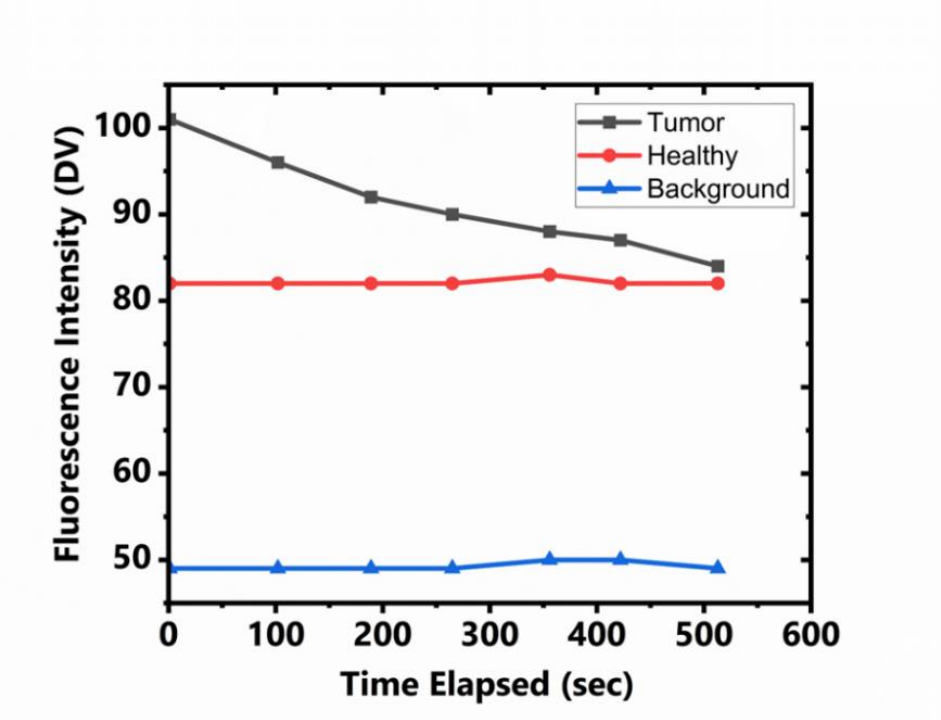

Figure 3.4- Fluorescence detected from ex vivo imaging of harvested tumor from lung cancer bearing mice by the endoscopic imaging system under continual exposure to irradiance of 100mW/cm^2 from three regions of interests- tumor, healthy tissues, and the background.

4 Design and preliminary evaluation of a highly sensitive endoscopic system for MIS fluorescence imaging

Lung cancer is the leading cause of cancer deaths in both men and women in the United States. According to American cancer society, it is estimated that there will be approximately 238,340 new cases of lung cancer and nearly 127,070 deaths from it in 2023. The survival rate is strongly influenced by the stage at which the disease is diagnosed, with earlier stages having a far better prognosis than later stages. For instance, the five-year survival rate for non-small cell lung carcinoma (NSCLC) treated at an early stage is 70-90% [9]. In contrast, the survival rate is nearly 6% when detected and treated in its advanced stage.

Video assisted thoracoscopic surgery (VATS), which was introduced in the 1990s, has been used increasingly for lung cancer treatment due to several benefits it offers including reduced postoperative pain, reduced incision, and shorter recovery time, among others [13,61]. While improvements in endoscopic imaging under white light illumination have contributed toward its success in the last 30 years, early detection of small or flat lesions could be quite challenging when the lesions exhibit indistinct morphological features when compared to the healthy surrounding tissues [62]. This could be a contributing factor for high post-surgical recurrence rates reported for lung cancers in several trials [18,63]. Minimally invasive surgeries (MIS) implementing color and near infrared (NIR) molecular imaging are emerging as a promising pathway to address these concerns. By labeling tumor cells with fluorescent probes that emit NIR light, surgeons can visualize the tumors as areas of increased fluorescence overlaid on high-resolution white light images of the anatomical structures. Furthermore, the use of NIR probes improves detection of deep-seated lesions due to the low absorption and scattering of biologic chromophores within 700-900nm wavelength range. As many advances are being made within the domain of tumor-targeting

probes, the specificity of cancer detection will continue to improve, thus holding a great promise for the future of fluorescence-based MIS for cancer treatment [27]. For instance, a novel cathepsin activated indocyanine green (ICG) probe (VGT 309) which remains fluorescently silent until it is activated in a tumor microenvironment where there is an upregulation of cathepsin has demonstrated improved specificity through various clinical trials.

Although MIS implementing molecular imaging offers several benefits, it can still introduce challenges that are almost non-existent in open surgeries. In the previous chapter, I pointed out one potential concern related to inadvertent probe exposure to excessive levels of excitation light irradiance during surgical maneuvering of the endoscope, which could cause photobleaching and raise the risk of overlooking cancerous lesions. Furthermore, the use of smaller diameter lens system in rigid endoscopes in comparison to systems used for open surgeries can further compound the risk by impacting the fluorescence sensitivity during endoscopic surgeries since the smaller diameter lenses have reduced light-gathering capacity. This becomes increasingly problematic when the system needs to detect weak fluorescence either from low probe aggregation at the targeted site or when the malignant lesion is seated deep under tissue surface.

One potential pathway to address these concerns is to employ a highly sensitive imaging sensor which would make it possible to detect fluorescence signals at low excitation intensities, thus reducing the likelihood of photobleaching. It would also allow for longer imaging sessions to potentially improve cancer detection by allowing more time to observe fluorescence signal. Recently, our group reported the development of a low read noise, high-dynamic range multispectral image sensor for image guided surgery [64]. It features high sensitivity in the NIR spectra and two readout chains which makes it feasible to detect low and high levels of photo charge using its high gain and low gain readouts respectively, making it a good candidate for NIR

fluorescence imaging in MIS. Additionally, an array of RGB-NIR bandpass pixelated filters that are integrated with the sensor enables it to simultaneously capture both color and NIR images.

In this chapter, I introduce an endoscopic system that incorporates the low noise CMOS imaging sensor along with a rigid endoscope that is optimized for high transmission of visible and NIR spectra with minimal chromatic aberrations. Several preliminary studies from benchtop to clinical trials have been conducted to evaluate the system performance. Firstly, I compare the sensitivity of the bioinspired endoscopic sensor (EIS) which was introduced in chapter 2 with this highly sensitive endoscopic system (HES) to ICG in three different concentrations prepared in vials to assess the level of improvement in sensitivity of the latter system under similar testing conditions. Next, I evaluate the system in a preclinical setting using a murine lung cancer model. ICG was administered 6 hours prior to *ex vivo* imaging of tumors and healthy tissues that were harvested post mice sacrifice. TBR from the detected fluorescence signals from the specimens was evaluated. Receiver operating characteristic (ROC) analysis was conducted to assess the effectiveness of the system to correctly discriminate tumors from healthy tissues. Lastly, clinical data from patients diagnosed with non-small cell lung cancer is presented. NIR fluorescence from the cathepsin-activated probe in the tumor site was imaged *ex vivo* in the operating room with the new system to assess its feasibility for clinical use.

4.1 System design

The HES comprises of the low noise imaging sensor, the endoscope, the light guide, and the light sources. The low-noise scientific CMOS camera features high sensitivity, high dynamic-range from its two readout channels which is critical for color-NIR fluorescence imaging, low read out noise, and pixelated spectral filters to enable simultaneous capture of both color and NIR fluorescence images. Additionally, it consist of a 10 mm rigid endoscope (OMEC Medical, San

Jose, CA, USA) and a custom bifurcated fiber cable (Sunoptic Technologies LLC, Jacksonville, FL, USA). The fiber cable was used to couple excitation light source (785 nm, R0785MU6000M4S, Innovative Photonic Solutions, Plainsboro, NJ, USA) and broadband LED visible light (UHP-T- WDS-DI, Prizmatix, Givat -Shmuel, Israel) into the endoscope's light post. The camera is coupled to the endoscope using a c-mount camera coupler. A notch filter was placed in the camera housing to suppress excitation from the 785nm laser (NF03-785E, Semrock). The image sensor is housed in a custom-built camera housing which was optimized for real-time data acquisition. All custom-printed circuit boards and camera housings are designed using Altium and Autocad software, respectively, and are fabricated by PCBWay (Shenzhen, China). A data acquisition board inside the camera housing (OpalKelly XEM 7310, Seattle, WA, USA) receives data from the image sensor using a low voltage differential signal bus and transfers the image data via a USB 3.0 interface to an external computer. Verilog language is used for the camera's firmware program. Data acquisition, image processing, and display are developed in Python, which enables real-time data acquisition and display on a Mac Studio (M1 Ultra processor, 128 GB unified memory, 8 TB solid state hard drive, Apple, Cupertino, CA, USA). Video data files are saved in h5 data format, which includes video data and various metadata information. The imaging system and the setup used for the studies is mostly equivalent to the depiction in Figure 2.3. However, in this instance, the bioinspired image sensor was replaced by the new low noise imaging sensor.

4.2 Comparing sensitivity of EIS with HES

In fluorescence imaging, weak fluorescence signals from low fluorophore aggregation at the tumor site may be difficult to detect and could impact the outcome of intraoperative surgery. This becomes even more problematic in MIS, where there is an increased likelihood of photobleaching the probe during surgical maneuvering of the endoscope. A high dynamic range endoscopic system

could offer a pathway to address these concerns as the fluorescence signal can be detected by such a system even when the irradiance is limited. To this end, I evaluated the sensitivity of the HES to ICG and compared the results against that of BIS which was introduced in chapter 2 under similar testing conditions.

ICG was prepared in serial dilution in three different concentrations (5 μM, 1 μM and 0.5 μM) in 1.5 ml vials. Phosphate buffered saline (PBS) was used as a negative control. The fluorescence signal was detected and captured by the image sensor upon excitation of the probe. The total output power of the 785 nm laser was set to 100 mW/cm^2 and the vial was placed 6 cm away from the distal end of the endoscope. Figure 4.1 displays the ratio of the digital value to the exposure setting (in log scale) to compare the sensitivity of HES and the EIS.

HES demonstrated about 58 times improvement in sensitivity in comparison to EIS for 5 μM and 1 μM ICG concentrations. At 0.5 μM, the digital values from EIS was in close proximity to the noise floor while HES demonstrated much higher sensitivity.

4.3 Murine lung cancer model

The performance of the HES was evaluated using a murine lung cancer model. Five female immunodeficient mice (J:NU, 2 months old, average weight 25 g; The Jackson Laboratory, Bar Harbor, Maine, USA) were used for *ex vivo* imaging and analysis. Each mouse was inoculated with A549 cells ($1X10^6$ cells per injection) into one of the mammary fat pads. When the tumor size grew to about $1cm^3$ in size, 100 μl of 100 μM concentration of ICG was administered into each mouse retro-orbitally. The mice were sacrificed 6 hours post dye administration. The tumor along with 2 healthy tissues were harvested from each mouse, providing a total of 5 tumors and 10 healthy specimens for *ex vivo* imaging and analysis. The output light irradiance from the

excitation source was set to 100mW/cm^2 and the HES collected fluorescence images at 50ms (~20 FPS). All animal experiments were performed under protocols approved by the University of Illinois Institutional Animal Care and Use Committee.

Figure 3 displays the representative color, NIR, and the overlay images captured from the tumor and the healthy tissues during *ex vivo* imaging from one of the mice. High levels of fluorescence from the tumor regions were observed during the imaging session as displayed in the image. The captured data was further analyzed using Matlab scripts.

A region of interest was selected from the tumors, healthy tissues, and the background to compute the level of detected fluorescence from the tumor and the healthy tissues from each of the mice. The tumor to background and healthy to background ratios were computed from each of the selected regions. Figure 4.3-A displays the ratios based on the classification (0 for healthy and 1 for tumor specimens)

A receiver operating characteristic (ROC) curve shown in Figure 4.3-B demonstrated an area under the curve (AUC) of 0.96 which indicates high ability of the system to accurately classify the specimen as tumor and healthy based on the detected fluorescence signal.

4.4 Back table imaging of human lung cancer nodules

Back table imaging of lung cancer from patients diagnosed with NSCLC was performed at the University of Pennsylvania using HES. All required authorizations were approved by the University of Pennsylvania Institutional Review Board. 24 hours prior to the surgery, 0.32 mg/kg of VGT-309 (Vergent Bioscience, Minneapolis, MN) was administered intravenously to six patients. The surgeon used a NIR intraoperative imaging system (VisonSense, Medtronic, Philadelphia, PA) to identify the location of the malignant nodules tagged by VGT-309 and

performed wedge-resection which contains the tumor and healthy tissue. Subsequently, HES with a 785 nm laser was used to image each nodule *ex vivo* on the back table. Afterward, the nodules were histologically analyzed to confirm their malignancy.

The captured images were processed and analyzed using Matlab. A region of interest was selected from the tumor and the healthy tissue. A high fluorescence signal was detected at the identified tumor regions reflected in the mean tumor-to-background ratio of 3.78 (ranging from 2.14 to 7.5) from eight specimens from the six patients. Figure 4.4-A displays the imaging setup utilized for the back table imaging of the wedge resection (Figure 4.4-B) resected from the patient. Tumor region is highlighted in false color from the detected fluorescence signal under NIR illumination.

The results from the preliminary clinical study demonstrate the feasibility of using the HES in a clinical setting.

4.5 Conclusion

In this chapter, I reported the design and evaluation of a highly sensitive endoscopic system that can address several issues raised when implementing NIR fluorescence imaging in minimally invasive surgeries for diseases like lung cancer where survival rate depends on the stage at which it is diagnosed and treated. Using a high-dynamic and low read noise image sensor and a highly optimized rigid endoscope, I demonstrated an improvement in the sensitivity of a commonly used dye- the ICG, when compared to the bioinspired endoscopic system introduced in chapter 2. I also presented the results from a murine lung cancer model where the system demonstrated a high receiver operating curve characteristic with an AUC of 0.96 for identifying tumor and healthy tissue specimens. I concluded the chapter by reporting the results from a clinical study where back table imaging of lung cancers, resected from patients who were administered with a cathepsin

activated ICG probe, was performed using the HES. A high TBR was observed from regions identified as tumor. Results from all the studies demonstrate high sensitivity and potential of the system to improve detection of cancers during minimally invasive surgeries with reduced likelihood of photobleaching the probes.

4.6 Figures

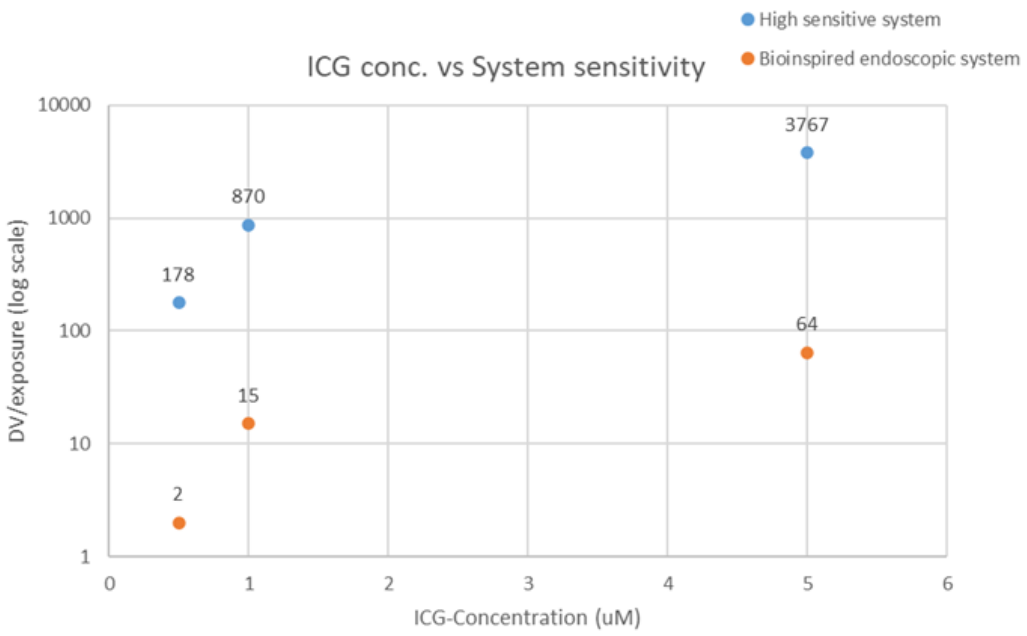

Figure 4.1- The sensitivity of HES and EIS is shown for three different ICG concentrations.

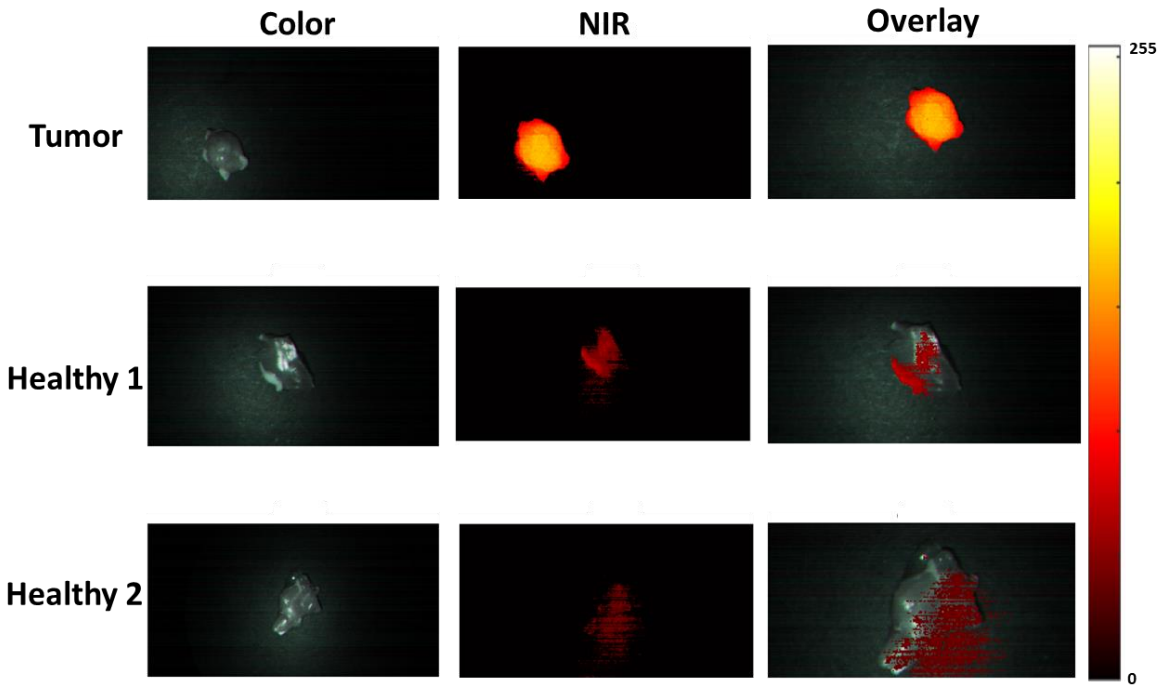

Figure 4.2- Ex vivo imaging of tumor and two healthy tissues from one of the mice. Image displays the color, NIR and the overlay images.

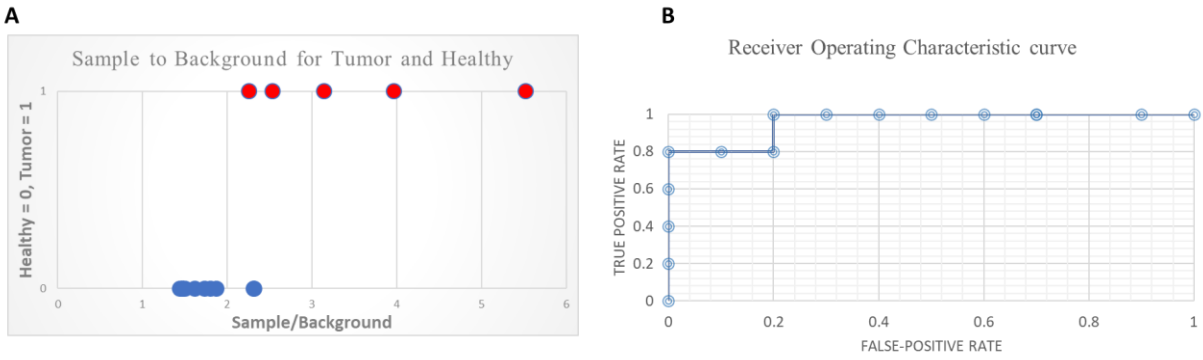

Figure 4.3- (A)The TBR computed from the tumor and the healthy samples during the ex vivo imaging of murine lung cancer model. (B) The Receiver operating characteristics curve from the study indicating high accuracy in classification of the specimen.

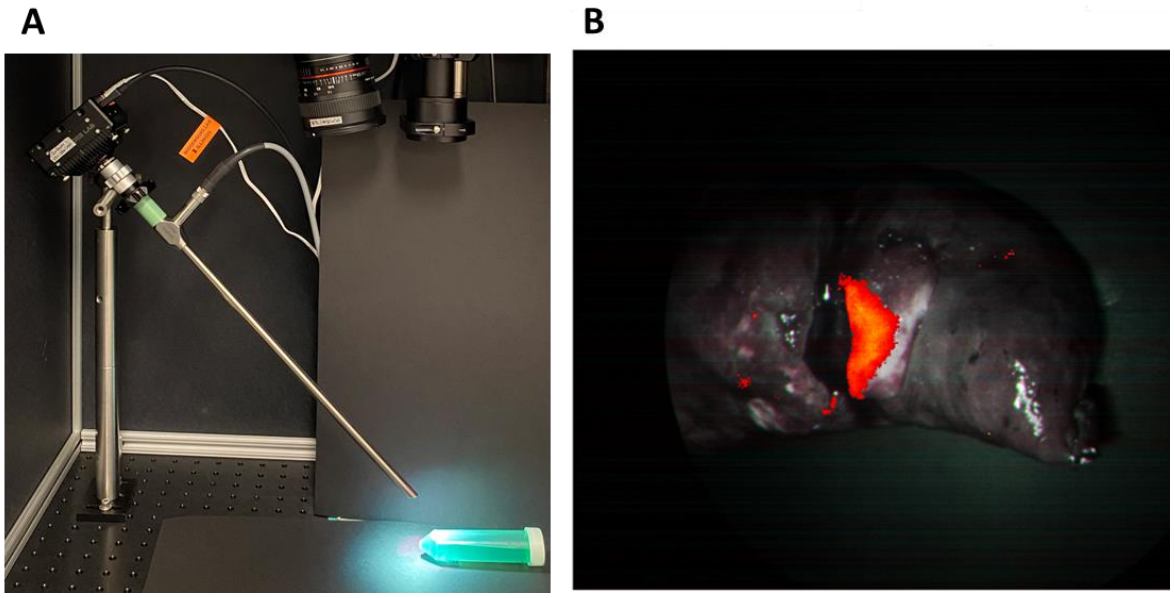

Figure 4.4-(A) displays the back table imaging setup of HES. (B) The wedge resection of the lung cancer containing both healthy and tumor. The tumor region was highlighted using NIR fluorescence image in false color.

5 Holographic imaging for fluorescence-guided surgery

Early detection of cancer is critical for five-year survival rates of different types of cancer [2]. Although pre-operative techniques such as MRI, PET, and ultrasound are improving the detection of early-stage cancer, there is often a disconnect between pre-operative surgical information and intraoperative procedures. This can often lead to difficulty in accurately localizing and identifying cancerous tissues during surgery and could result in incomplete tumor resection or damage to surrounding healthy tissues. Surgeons rely on their sight and touch as primary sensing modalities during surgeries, and often the success of the surgeries is dependent on their experience. Incomplete cancer resection remains a common problem in many types of surgical procedures, as small cancerous tissues and margins can blend easily with healthy tissue. Unfortunately, this can result in a poor prognosis for patients, as evidenced by up to 25% of breast cancer patients, 35% of colon cancer patients, and as many as 40% of head and neck cancer patients experiencing incomplete resection [4–7].

The utilization of intraoperative near-infrared fluorescent-guided surgery has shown significant promise in addressing these challenges to enhance patient outcomes. The success of this modality relies on three essential components: tumor-targeted probes, illumination, and imaging devices and display unit [21,59]. Tumor-targeted probes have driven this field from the research lab to the clinic, starting with ICG and methylene blue (MB) fluorophores for angiography, delineation of tumors due to passive accumulation, and mapping of sentinel lymph nodes in patients with cancer [65]. Additionally, many tumor-targeted probes are in phase three clinical trials or have completed them, and commercialization is imminent [66,67].

Concurrently, advances in imaging sensors and illumination devices have also significantly improved the performance and capabilities of fluorescence imaging in cancer surgery. For

example, miniature imaging sensors have enabled high-resolution, real-time imaging in both visible and NIR spectrums for both open and minimally invasive surgeries [68]. Each new generation of sensors typically brings improvements in several key performance metrics. This includes quantum efficiency, dynamic range, readout rates, and signal-to-noise ratio, which enables capture of high-quality images even in low light conditions. Among illumination devices, laser diodes have been traditionally used as the excitation source. However, bright, narrowband NIR light-emitting diodes now provide a cost-effective alternative [69].

Tumor-targeted probes, intraoperative imaging, and illumination devices are critical for real-time detection of cancerous tissue in the operating room. However, displaying this information in a time-sensitive manner without interrupting the surgical workflow is equally crucial. Currently, most preoperative imaging instruments use regular monitors, which are also common in the surgical suite. Surgeons generally undergo rigorous training to perform surgeries using information displayed on regular monitors, but the loss of depth information can lead to iatrogenic damage, prolonged surgical time, and incomplete tumor resection. Wearable goggles offer a partial solution to this issue by providing color and NIR fluorescent information in the operating room without shifting the focus away from the surgical site. However, they replace natural eyesight with virtual reality, which can disrupt the natural surgical workflow and has its own drawbacks [70–73].

I have developed an intraoperative imaging system using holographic goggles to address issues related to real-time fluorescence imaging and depth display information. Mixed reality holographic goggles utilize see-through glasses to provide natural vision and computer-generated visual information displayed via spatial light modulators to both eyes, creating 3D augmented reality with some disparity as illustrated in Figure 5.1. The holographic goggles are equipped with an inertial an inertial magnetic unit, which records the user's head movement and enables the

augmented reality to be updated based on the user's gaze direction. The system generates augmented visual data about the location of the tumor by capturing NIR information using a bioinspired, single-chip multispectral imaging sensor. This visual information is calibrated and co-registered with the operator's natural eyesight, allowing for the surgical site to be viewed using natural eyesight but enhanced with artificial information which indicates the location of the tumor highlighted by the fluorescent molecular markers. The system also displays preoperative images near the surgical wound site, allowing for easy access with minimal head movement. In this chapter, I present data that quantifies the accuracy improvement for fluorescent targeted localization with the 3D holographic system in comparison to 2D display monitor using phantoms. Furthermore, I also present results from preclinical studies using the system.

5.1 Features offered by holographic goggles that are optimal for FGS

In this section, I will highlight several key features offered by the mixed reality holographic googles that are optimal for FGS.

5.1.1 Offering mixed reality experience

One of the key features that wearable display systems like HoloLens offer is the provision of Mixed Reality (MR) experience where the user can have access to both the real world and the virtual world simultaneously. The see-through displays enable access to the real world via the user’s natural vision, while the fluorescent images could be displayed as holograms. This radically enhances the surgeon’s visual perception of the 3D scene compared to 2D displays where an external camera with lower color resolving power compared to the human eye is utilized to capture visible images from the scene. Typically, the captured images undergo color corrections to reproduce color perception like the human eye before they are displayed. However, the color-corrected images may still differ from how the user perceives the target in the real world which

could negatively impact the surgery due to possible feature misrepresentation or even misidentification. The see-through displays can eliminate these inconsistencies.

5.1.2 Matching user field-of-view

By co-registering the virtual fluorescent with the natural vision, the position of the hologram, as perceived by the observer, is preserved and independent of any rotational and translational motion. In contrast, the images displayed on 2D monitors remain static and do not reflect the perspective variations that are caused by user motion. The field of view (FOV) in 2D displays is dependent on the camera position and orientation relative to the target which may significantly differ from the surgeon's perspective of the surgical site and could contribute to an increased cognitive workload from the execution of mental transformations to compensate for the differences [33].

5.1.3 Stereoscopic vision

An additional feature that the holographic displays offer to enhance surgical guidance is the provision of stereoscopic vision using its two see-through holographic display screens. Binocular depth cues include stereopsis (the ability of the brain to use differences between the images received by each eye to perceive depth) and convergence (inward movement of the eyes as an object comes close to the viewer). These cues allow for more accurate and natural perception of depth in the real world. This feature creates an illusion for the user that the fluorescent images are superimposed on the actual target.

5.1.4 Less interruptions during surgical procedure

As indicated previously, Holographic displays offer the additional benefit for the surgeon to proceed the surgery with minimal interruption, since the fluorescence image is displayed as hologram on the optical see-through displays while having simultaneous visual access to the

surgical site via natural vision. In contrast, the use of 2D displays requires the surgeon to frequently halt the procedure to access the fluorescence signal.

5.1.5 Multi-modal imaging display capabilities

The application which runs on the display could be designed to display other imaging modalities, for instance preloaded CT images, in addition to fluorescence images. Traditionally, different imaging modalities are displayed on different display screens. The design of the display application to cater to various surgical requirements could save space in the operating room.

5.2 System design and setup

The holographic intraoperative system is comprised of the bioinspired single-chip multispectral imaging sensor which was previously introduced in chapter 2, holographic goggle (Microsoft HoloLens), laser light illumination (BWF2-780 and BWF2-660, B&W TEK, Plainsboro, NJ, USA), personal computer (Lenovo M Series Tiny PC, i7 Intel Pentium, 16 GB RAM), wireless router (R6220, Netgear, San Jose, CA, USA) and custom printed circuit board equipped with near infrared LEDs for optical calibration and co-registration. The architecture of the image sensor is inspired by the evolved visual system of the mantis shrimp. Every pixel feature three vertically stacked photodetectors (Top, Middle and Bottom), each with a distinct spectral response that gives the sensor its spectra resolving capabilities. Furthermore, the pixels are overlaid with two distinct pixelated spectral filters to simultaneously capture and separate visible and NIR images in real-time (Figure 5.2-A).

All printed circuit boards and the camera housing were designed using Altium or Autocad and fabricated by PCBway (Shenzhen, China). The FPGA firmware was developed using Xilinx Verilog, and the data acquisition and display software was written in programming languages such

as Python and C++. The mixed reality application was developed using Unity game engine and visual studio toolkit. Flat sprite was utilized as hologram to project the fluorescence image retrieved by the display system.

The data from the image sensor is streamed to a PC, where additional signal processing is performed, such as image calibration, co-registration with the natural eyesight, color compression and wireless streaming of data to the holographic goggles (Figure 5.2-B). The application which runs on the device can display 24-bit color images. However, since high color resolution images require long transmission time of over 100 msec and introduce image lag, I explored the option of reducing the bit depth of the color images while still displaying the necessary contrast information to the surgeon under 50 msec from end to end.

A threshold is applied to the acquired NIR image, and only pixels with digital values above the threshold are displayed in false color. Pixels below the threshold are represented as black color and are rendered transparent on the display. Hence, the operator can view the surgical site with their natural vision while only fluorescent information above the preset threshold is augmented to the natural eyesight. The threshold level of the near infrared can be altered during the surgery to accommodate for the operators' preferences. The compressed color image is transmitted wirelessly to the holographic goggles, where an embedded processor generates a false-color hologram and projects on the binocular display.

5.3 Hologram co-registration with natural vision

To ensure accurate and precise visualization during surgery, the holographic intraoperative system requires calibration and co-registration of the NIR image with the hologram projected onto the see-through display screen. The process involves two steps. First, a custom printed circuit board

with four NIR light-emitting diodes (LEDs) placed in known positions is imaged using the bioinspired imaging sensor. A threshold is applied to the NIR image and the locations of the four LEDs are determined in the image by analyzing the contours and first moments of the pixels. OpenCV APIs are utilized by the custom C++ software to locate the contours and the first moment of each of these LED regions [74]. A homography matrix is then computed using the first moment and pixel locations as input. The matrix is then applied to all new frames acquired from the image sensor. The resulting hologram is then wirelessly transferred to the holographic goggles and displayed to the user. In our previously published study [75], affine transformation was utilized for the co-registration algorithm. However, since this transformation preserves line parallelism, it places stringent constraints on the position of the image sensor relative to the plane of the calibration board as it cannot address perspective distortions. I was able to address this concern by implementing perspective transformation, which relaxes the position and orientation requirements for the image sensor.

The second step involves the operator placing the hologram on the calibration board such that the visual information from the LEDs is correctly superimposed with the hologram. This is achieved using a series of voice and gesture commands that are recognizable by the holographic goggles. As each user has a unique disparity, this step can be time-consuming to ensure the correct co-registration. This critical process ensures that the augmented reality provided by the system accurately aligns with the natural eyesight of the operator, enabling them to precisely locate and remove cancerous tissues.

Figure 5.3-(A-E) displays the various stages of the calibration routine. At first, the hologram is positioned and aligned inside the perimeter of the calibration board (depicted in Figure 5.3-A), which consisted of four NIR LEDs located at predetermined relative positions. Next, the NIR

signals from the LEDs were captured by the image sensor (Figure 5.3-B). The contours of each of the detected regions are displayed in Figure 5.3-C which is used to compute the homography. After calibration, the hologram is accurately co-registered with the locations of the LEDs on the board. Figure 5.3-D and Figure 5.3-E display the composite image of the calibration board and hologram before and after the co-registration routine, respectively. Figure 5.3-F shows the outcome of the co-registration routine using a vial of excited quantum dots. The fluorescent signal displayed in false green color accurately mapped the location of the quantum dots within the vial.

An experiment assessing co-registration errors between holograms and the real-world at varying depths was also carried out. Although the holographic goggle provides a 3D mesh of the real world, it lacks the necessary spatial resolution for intraoperative procedures. Therefore, I utilized a planar hologram that was positioned at a fixed distance from the user which results in co-registration errors that varied based on the changes in the offset from the target. To evaluate the errors, the calibration printed circuit board was placed at a certain depth after calibrating and co-registering the imaging system. The distance of the hologram was incrementally adjusted above and below the initial calibration plane in 5mm increments, while the operator's viewing angle remained fixed at approximately 60 degrees.

The equation below describes the mathematical model that quantifies the co-registration error (e_i) between the real-world point P_i and its projection on the hologram P_i', as a function of the hologram's offset from the calibration board plane (h_i) and the operator's viewing angle (θ) relative to the plane:

$$e_i = \frac{h_i}{tan\ \theta}$$

Figure 5.4-A illustrates an error model that describes how co-registration of natural vision with the hologram deteriorates as a function of hologram offset from the calibration board plane and the view angle relative to the same plane. The result of the theoretical error computed from the equation above and the co-registration error is displayed in Figure 5.4-B. The distance measured between a specific LED on the calibration board in the real world and the corresponding area in the hologram in increments of 5 mm offset above (>0) and below (<0) the calibration plane was used to monitor the error. The view angle was maintained approximately at 60°.

A good correlation was observed between the model and the observations from the study. The co-registration error linearly increased as a function of the offset of the hologram from the calibration board. The results show roughly 2 mm of co-registration error within a 5 mm offset. The error is minimized, regardless of the offset from the calibration plane, as the operator's view angle approaches 90°.

5.4 Hologram color rendering for real time visualization of fluorescent images

One of the design goals of the system was to display the captured NIR image on the HoloLens with minimal delay. To this end, the quality of the virtual image displayed on the holographic goggles after different levels of compression was evaluated. A 24-bit horizontally modulated gradient image (excluding the alpha channel) was generated in the main software. It was then compressed to 12-bit and 6-bit images by extracting the most significant bits and then transmitted to the goggles for display. Mixed reality capture was used to record the hologram displayed on the goggles and assess both the quality of the color gradient image after compression and the transmission time between the PC and the goggles for real-time display.

The original 24-bit image displayed a wide color range with seamless transitions between colors (Figure 5.5-A). The hologram captured using the mixed reality capture tool, demonstrated that the system could preserve image quality when the original 24-bit image was compressed to 12-bit, as the color transitions appeared continuous (Figure 5.5-B). However, when the image was further compressed to 6-bit (Figure 5.5-C), significant degradation in image quality was observed with discrete transitions between colors. In a surgical setting, it is essential to display a wide color gamut to differentiate regions with high fluorescence from those with low fluorescence. Qualitatively, I demonstrated that we were able to achieve this requirement satisfactorily with 12-bit compression, resulting in an average delay of 50 milliseconds between image capture and display on the goggles. Consequently, 24-bit to 12-bit compression scheme was adopted for all the studies.

5.5 FGS simulation study

One of the advantages of the holographic imaging system is the improved accuracy in identifying and localizing targets compared to traditional imaging systems that rely on 2-D display monitors. The system provides enhanced depth perception, allowing for better visualization of the surgical site with natural eyesight. To evaluate the impact of 2D display monitors on depth perception during fluorescent-guided surgery, as study using six 3D-printed phantoms with varying levels of hills and valleys was conducted. The phantoms were painted black to minimize visual cues to identify the 3D topology (Figure 5.6 -A). Each valley was filled with a 100 µL concentration of ICG diluted in PBS (10 µM), which fluoresced under 780 nm laser excitation (20 mW/cm2) and was detected by the bioinspired image sensor.

Four participants with clinical backgrounds were asked to locate and delineate the fluorescence margin on each of the phantoms using a pointed Sharpie, either by viewing information displayed on a 2D monitor or by using our 3D holographic system. To eliminate any visual biases towards

the target that may assist in its delineation, a small curtain was placed between the operator and the phantom when fluorescent information was displayed on the 2D monitor, to limit depth perception to monocular depth cues. The distance between the participant's estimation of the target location and the actual depth was recorded for each phantom. Each operator was randomly assigned a phantom, and the fluorescent information was presented either on the 2D monitor or on the 3D holographic goggles. The experimental setup addresses two potential surgical scenarios. Firstly, during open surgeries that rely on fluorescence guidance, the surgeon typically performs most of the surgery while observing the 2D monitor. Secondly, in minimally invasive surgeries, the surgeon lacks the depth cues obtained through natural eyesight. Therefore, the phantom study provided a simplified testing ground for evaluating the accuracy associated with display technology in fluorescence-guided surgery.

The mean and standard deviation of the estimation error are plotted in Figure 5.6 -B, which was obtained after measuring the distance between the actual location of the ICG solution in the phantom and the participant's estimate of its location. The plot shows the estimation error for each phantom as a function of the valley depth. The results demonstrate that the participants were able to locate and delineate the fluorescence signal accurately when the valley depth was shallow, resulting in minimal errors. However, an increase in the valley depth led to a proportional increase in the error, indicating impairment of the participant's depth perception. In contrast, the holographic goggles featuring stereoscopic vision reduced the error since they provide binocular depth cues that resemble the human visual system in a natural environment.

5.6 Small animal model for breast cancer

Recent developments in tumor-specific probes have resulted in remarkable improvements in surgical outcomes due to enhanced detection, margin control, and survival of patients diagnosed

with different types of cancers. Therefore, a versatile FGS system must demonstrate high sensitivity to complement a wide range of clinical and pre-clinical probes to adapt to different intraoperative procedures. Herein, the system's ability to detect various commercially available non-specific (ICG) and tumor-targeting NIR probes (IRDye 800CW 2DG and RGD) in tumor-bearing mice was demonstrated.

Eight female immunodeficient mice (J:NU, 2 months old, average weight 25 g) were purchased from the Jackson Laboratory (Bar Harbor, Maine, USA). Each mouse was inoculated with 4T1 mammary carcinoma cells ($1x10^6$ cells per injection) orthotopically into the mammary fat pad. When the tumors grew to 1 cm^3 in size, each mouse was intravenously administered with one of the following NIR fluorescent dyes: IRDye 800CW, IRDye 800CW 2-DG, IRDye 800CW RGD, and ICG. At 6 hours post-administration, each mouse was placed on a stage with a heating pad (37 °C) where anesthesia was maintained using mask inhalation with 1.5-2.0% isoflurane. All animal experiments were performed under protocols approved by the University of Illinois Institutional Animal Care and Use Committee (IACUC, Protocol ID 20194). The 780 nm laser (20 mW/cm2) was utilized for excitation. The exposure setting of the system was configured depending on the characteristics of each dye. The visible images superimposed with the NIR-fluorescence images were captured using the mixed reality capture tool. Although the surgical site was accessed via natural vision using the goggles' see-through display, the color camera mounted on the front of the device was used to capture the visible images for illustration purposes.

Figure 5.7-A displays the composite image of the mouse injected with IRDye 800CW with light sources turned off and on demonstrating accurate co-registration between the fluorescence from the hologram and the location of the tumor in the real world. The position of the hologram, as perceived by the user, is preserved and is independent of any rotational and translational motion

where the coordinates of the co-registered hologram remained unaltered relative to the position of the tumor accessed by the natural vision regardless of the perspective changes.

After the in vivo imaging, the mice were euthanized to harvest the tumors and the adjacent muscle tissues for ex vivo imaging using the HNFI system. Later, 10 μm-thick specimens were obtained, stained with hematoxylin and eosin (H&E), and imaged with an optical slide scanning system (Nanozoomer slide scanning system, Hamamatsu, Japan). The ex vivo biodistribution study shows that all harvested organs exhibited different levels of fluorescence to depict the preferential accumulation of the dyes at the tumor site and their clearance pathway via the liver and kidneys (Figure 5.7-B). The histological images of H&E-stained specimens of a tumor and healthy muscle tissue depict the different cellular and tissue structures contributing to high contrast in fluorescence between the two. Representative in vivo fluorescence images in Figure 5.7-C depicts the capability of the system to detect and display the location of the tumors with different types and doses of NIR fluorophores, indicating that the system could be easily utilized for various clinical applications.

5.7 Conclusion

In this chapter, I highlighted some of the challenges with using 2D monitors which are commonly employed as displays for fluorescence guided systems. One of the main concerns is associated with the loss of depth information that can lead to iatrogenic damage, prolonged surgical time from interruption in surgical workflow, and incomplete tumor resection. To address this, I introduced an intraoperative system incorporating the bioinspired image sensor and a holographic display system which features optical see-through display screens. Using this system, the surgeons can access both the surgical sight using natural eyesight and the location of the diseased tissues using the fluorescence signal captured by the system and projected on the display as hologram. Through a series of experiments with 3D-printed phantoms and small animal models of cancer, I showcase

the benefits of the system. Results indicate that using holographic display technology has the potential to significantly enhance surgical accuracy and efficiency.

5.8 Figures

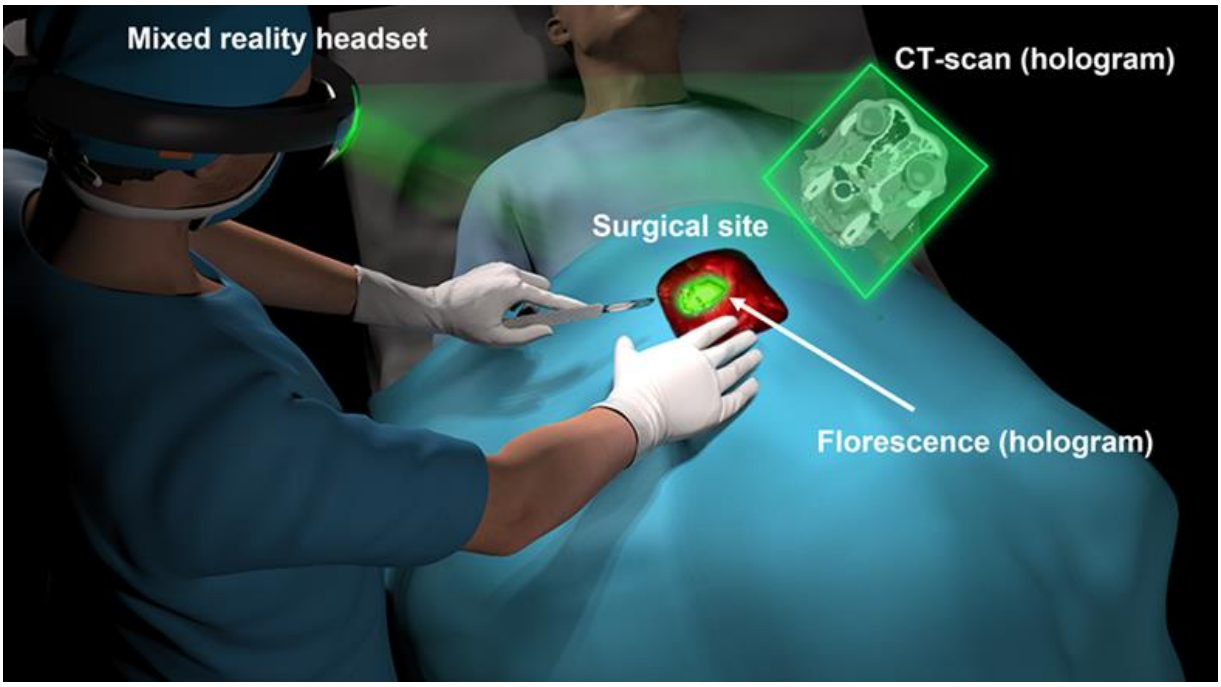

Figure 5.1- Illustration of our intraoperative holographic imaging system, which includes a bioinspired single-chip multispectral imaging sensor, a laser light excitation source, holographic goggles, and a computer for data acquisition and image processing. The system enables visualization of the surgical site with natural eyesight and augmentation of holograms indicating the location of tumor tissue marked by fluorescent molecular probes.

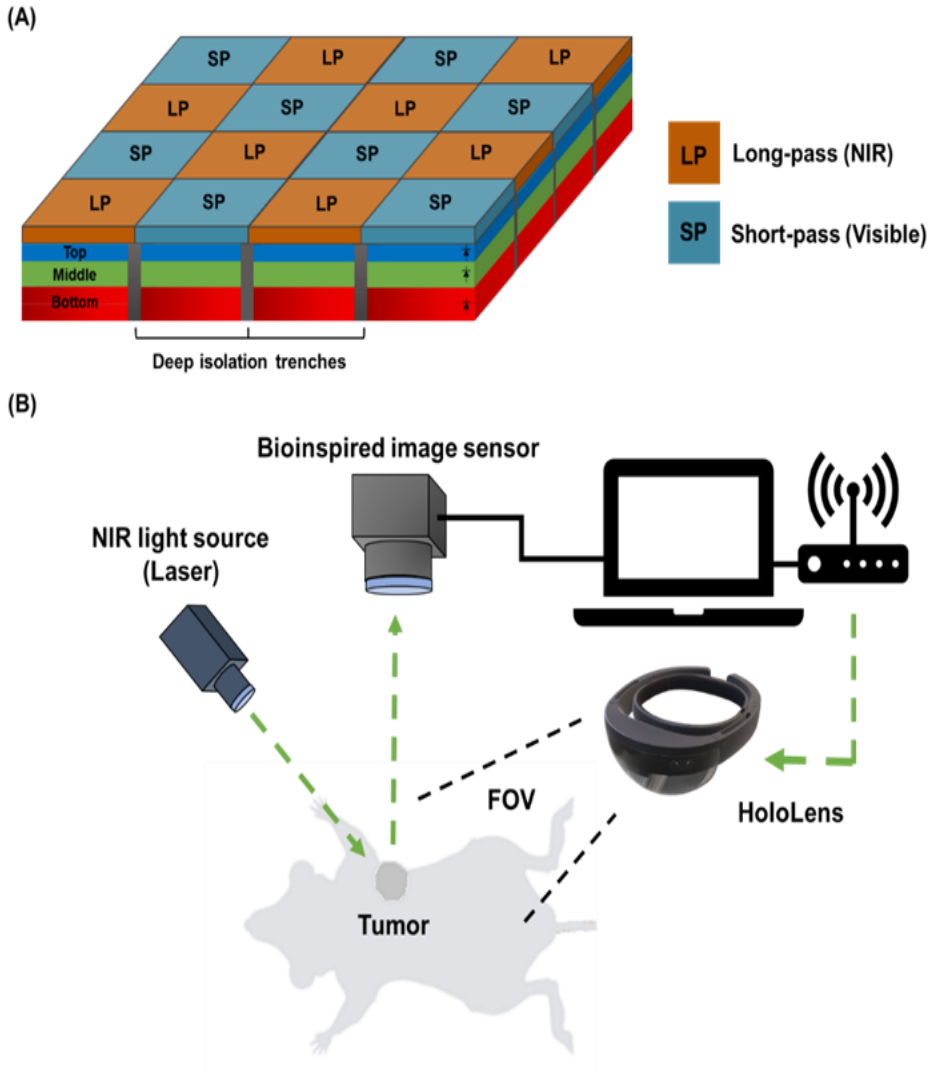

Figure 5.2- Schematic illustration of FGS with the bioinspired image sensor and HoloLens showing (A) the pixel array of vertically stacked photodiodes showing the top, middle, and bottom layers of the photosensitive cells in blue, green, and red, respectively, and (B) the experimental setup of the HoloLens system utilized for the in vivo imaging of tumor-bearing mouse.

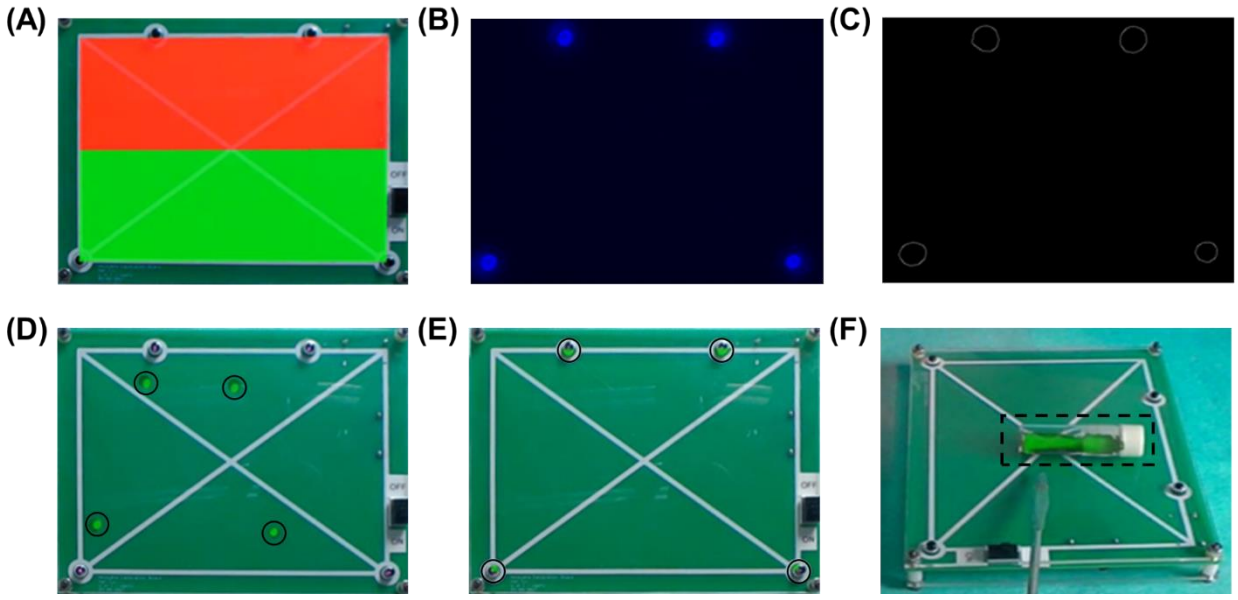

Figure 5.3- Various stages of the Calibration procedure for co-registering a virtual image with the natural vision. (A) Image displays the hologram with the default image after being positioned within the real-world calibration board borders. (B) The bioinspired camera detects four NIR LEDs mounted on the calibration board. (C) Contours of the detected NIR regions. (D) Illustration of co-registration before calibration and (E) after calibration. (F) A vial containing quantum dots demonstrates co-registration post calibration.

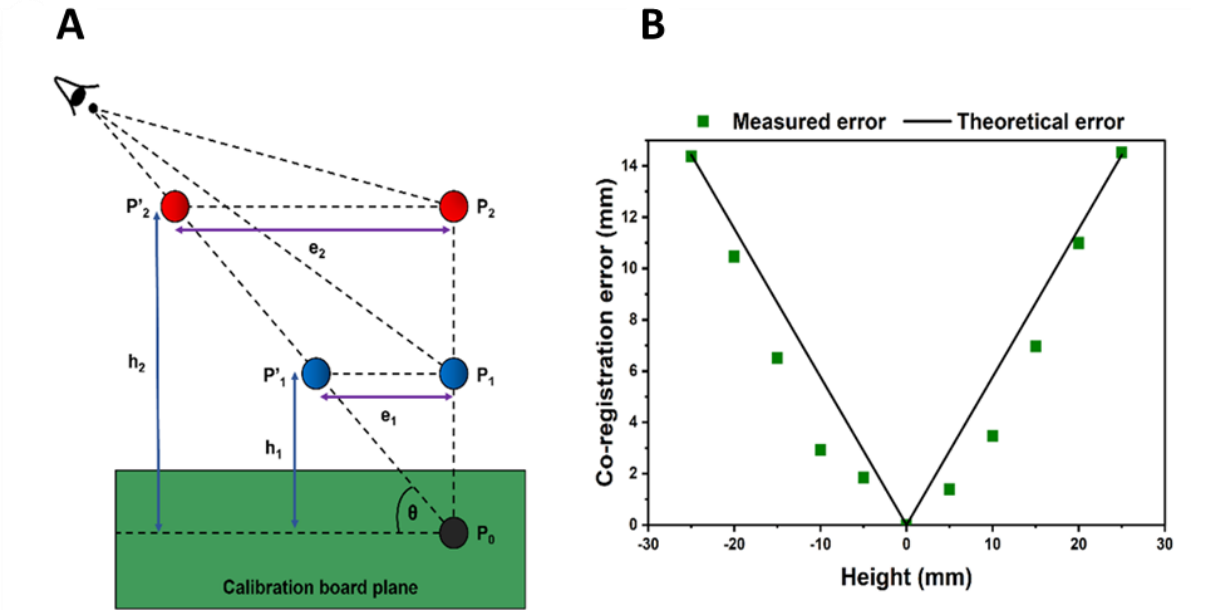

Figure 5.4-(A) Co-registration error model displaying the dependence of error (e_i) on an offset from calibration plane (h_i) and the viewing angle (θ). (B) Comparison of error computed from the error model and the results obtained from the chessboard pattern placed at different offsets from the calibration board plane.

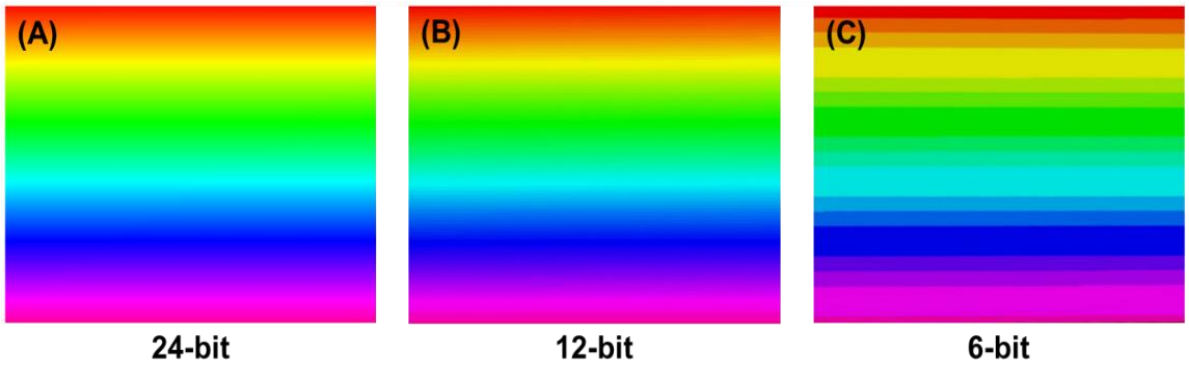

Figure 5.5- Color gradient image with different bit widths displayed on the HoloLens. (A) Pre-compressed original image with 24-bit image depth, (B) Image after compressing the image to 12-bit depth and (C) Image after compression to 6-bit image depth.

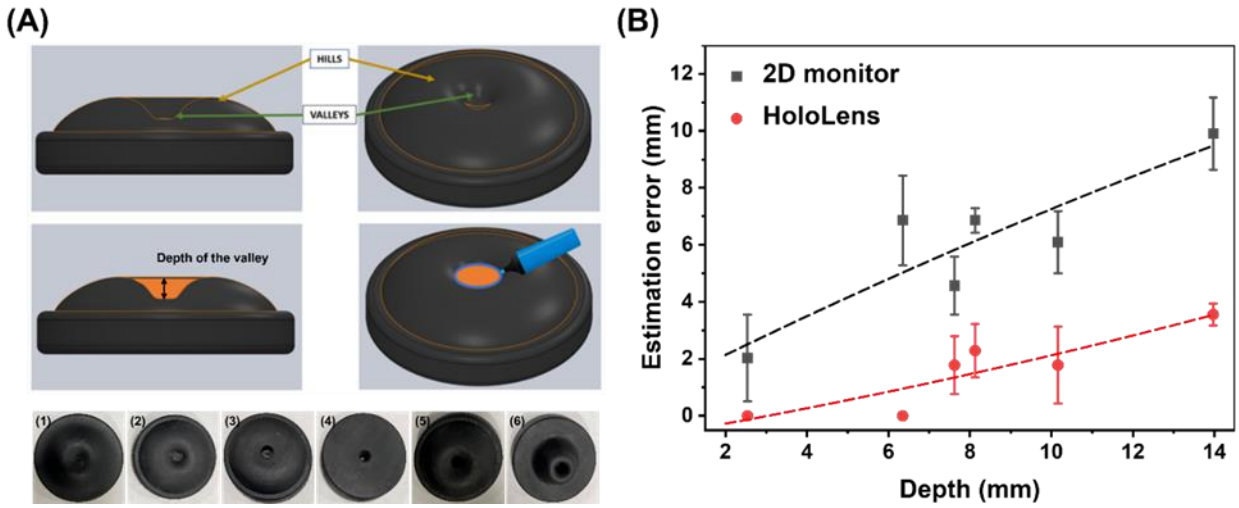

Figure 5.6- (A) Phantoms with varying valley depths used in the fluorescence guided surgery (FGS) simulation study. The bottom image shows the phantoms arranged in increasing order of valley depth. (B) Results comparing estimation error of fluorescent dye location using the 2D monitor and the holographic goggles. The plot shows mean and standard deviation of the error for each phantom as a function of valley depth, indicating that holographic goggles with stereoscopic vision offer better depth perception compared to 2D monitors.

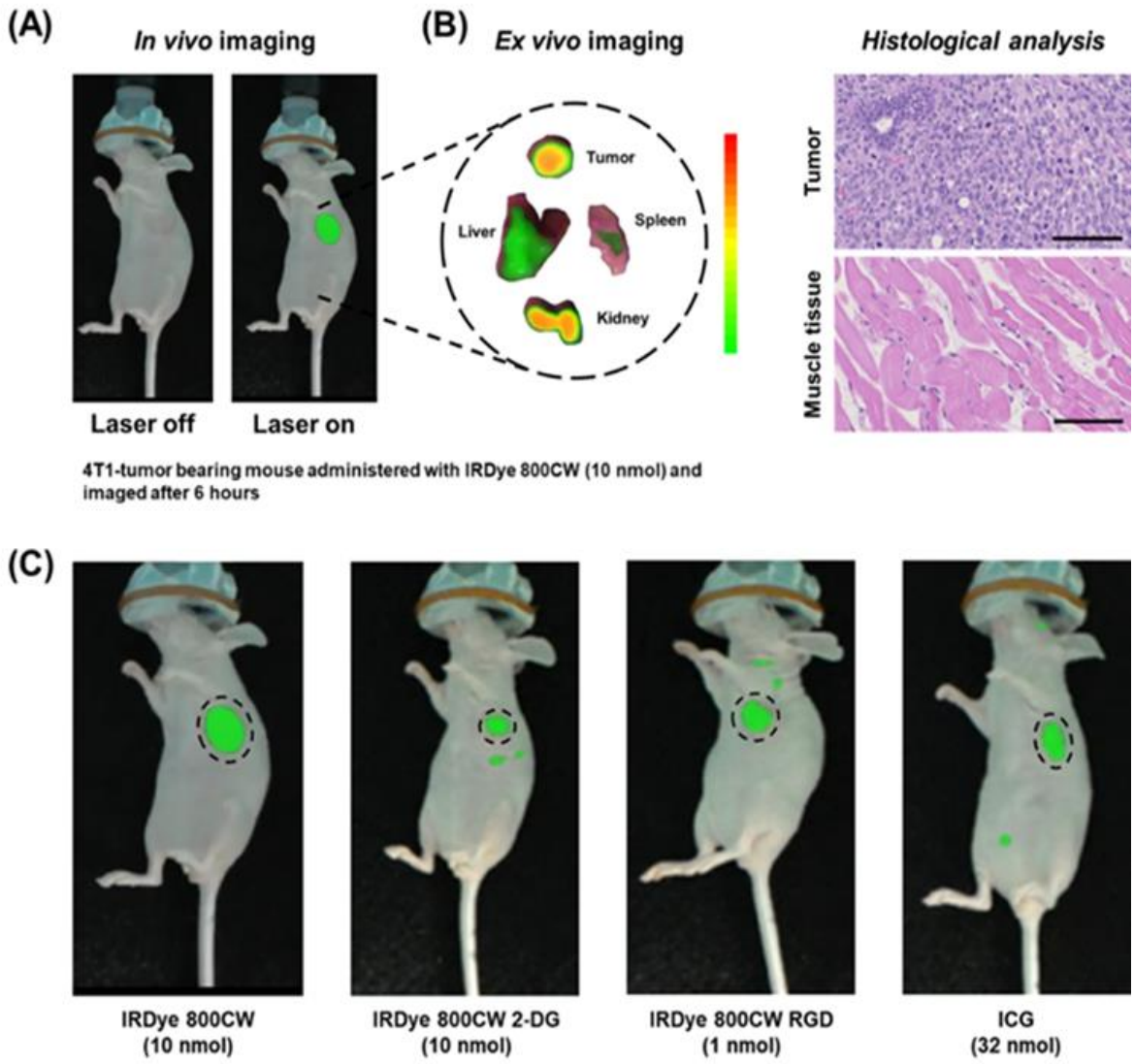

Figure 5.7- In vivo and ex vivo imaging using the HoloLens. (A) Fluorescence image of tumor-bearing mouse displayed on the HoloLens with excitation source turned off and on. (B) Corresponding ex vivo fluorescence image of resected tumor, liver, kidneys, and muscle tissue with Histological image of H&E-stained specimen of a tumor and muscle tissue. Scale bar: 100 µm. (C) In vivo fluorescence images of mouse models captured by the HoloLens 6 hours post-administration of IR800CW (10 nM), IR800CW-2DG (200 µM), IR800CW-RGD (20 µM), and ICG (640 µM).

6 Concluding Remarks and Discussion

In the last 50 years, there has been a substantial change in the way surgeries are conducted, and numerous technological advancements have played a significant role in this transition. One of the significant changes we have witnessed is the focus on minimizing surgical trauma to facilitate the recovery of patients after the surgery. This has led to the development and adoption of minimally invasive surgical techniques for surveillance and treatment of several cancer types since they foster speedy recovery, lessen blood loss, reduce patient risk, and minimize cosmetic damage [76,77]. Although minimally invasive surgeries enhance the visualization of critical tissues, endoscopic imaging under white light illumination is severely limited in its ability to detect flat or deeply seated cancerous lesions due to insufficient morphological differences compared to healthy tissues, which can lead to unfavorable clinical outcome.

Fluorescence guided surgery (FGS) using NIR probes has addressed these concerns by providing intraoperative visual feedback on the location of the tumor to the surgeon. Since its inception, it has evolved over the years, thanks to many groundbreaking advances, and has now expanded to various surgical specialties and cancer types, including breast, lung, and prostate cancers. Recently, we have witnessed a plethora of probes that have entered clinical trials with potential for translation [27,78,79]. For example, the first in-human fluorescence imaging of glioblastoma using fluorescently labeled cetuximab-IRDye800 which targets the EGFR receptors was recently reported [80]. Another instance of targeted probes utilized in FGS is the use of a novel antibody (3E8 Mab) conjugated with IRDy800CW to target TAG-72 in colorectal cancer [81]. Combining these NIR probes with MIS is emerging as a promising approach with the potential to enhance patient outcomes as tumors can be visualized as areas of increased fluorescence on top of high-resolution white light images of anatomical structures. However, despite the benefits this

multimodal platform brings, there are several limitations that could hinder its effectiveness. My research contributions attempt to identify and address these limitations.

One of the obstacles involves the use of a single molecular tracer to detect cancers which are often characterized by heterogeneity which can limit tumor detection rates. For example, ~80% of lung adenocarcinomas have high expression of folate alpha receptors and will benefit from Pafolacianine dye to highlight the location of tumors during surgical procedures [82–84]. It has been clinically demonstrated that in this patient population, unplanned secondary tumor nodules were identified in ~50% of the patient, attesting to the benefits of FGS. Although a five-year disease-free survival rate is still unknown for patients undergoing FGS with Pafolacianine, the improved detection rate of secondary tumors provides optimism toward a better clinical outcome. However, about ~20% of adenocarcinoma patients and the majority of squamous cell and non-small cell lung cancer patients will not benefit from the Pafolacianine probe due to a lack of folate alpha receptors in the primary tumors. Enzyme- or pH-activated probes have the potential to address some of these shortcomings, as demonstrated by results from phase 2 and phase 3 clinical trials, though none of these probes are FDA-approved at this time. Since there is still no universal molecular probe that works for all types of cancers, one potential pathway will involve the use of a cocktail of carefully selected tracers to highlight tumors with increased specificity.

Current state-of-the-art endoscopic imaging instruments are typically optimized to image single NIR probe. However, the single molecular probe approach comes with its own deficits including highlighting healthy tissues as tumors (false positives) and missing tumors (false negatives) due to inter- and intra-tumor heterogeneity. Combining multiple tumor-specific tracers can reduce the false positive and false negative detection rates while also increasing the confidence in the true negative and true positive signals by accumulating in the tumors together and avoiding healthy

tissue. In order to improve tumor detection sensitivity and specificity, an imaging instrument should be able to detect and differentiate the fluorescence from multiple molecular probes. Aggregating the fluorescence from different probes without individually differentiating them will dampen the strengths of the individual probes to detect tumors and avoid surrounding healthy tissue.

To address this, I have developed a bioinspired endoscopic system that combines a single-chip multispectral imaging sensor with a highly optimized rigid endoscope that features transmission of visible and NIR spectra with minimal loss and chromatic aberrations. The imaging sensor developed in our lab is bioinspired and is radically different from the conventional image sensors. The pixel architecture models after the visual system of mantis shrimp and combines three vertically stacked photodetectors with two pixelated spectral filters arranged in a checkerboard pattern, enabling the sensor to make three observations in the NIR spectra while simultaneously capturing visible (color) images. The spectral response for each of the vertically stacked photodetectors is unique and enables it to discriminate multiple fluorophores. When combining a single-chip multispectral camera with a rigid endoscope, it is crucial to carefully design the endoscope to ensure that both NIR and color images are focused on the same focal plane. Failure to do so may result in decreased fluorescence sensitivity and reduced spatial resolution. Using tests from benchtop, preclinical and clinical studies which are elaborated in chapter 2, I have demonstrated the system's ability to detect and differentiate multiple fluorophores while at the same time feature minimal chromatic aberrations.

Another obstacle that is often overlooked when implementing NIR fluorescence imaging in MIS is related to accidental photobleaching of the probe due to increased levels of irradiance during surgical maneuvering of the endoscope. This can lead to a negative outcome for the patient, as the

probe may not highlight the presence of cancer during the surgery due to photobleaching. Furthermore, detection of weak fluorescence signal becomes a critical system requirement in the context of MIS. Most endoscopes utilize smaller diameter lenses to reduce their overall size, which can enhance their maneuverability during surgery while minimizing damage to surrounding tissues. However, this comes at the cost of reduced light gathering capacity, making detection of weak fluorescence signals more challenging. It becomes increasingly problematic when the system needs to detect weak fluorescence either from low probe aggregation at the targeted site or when the tumor is seated deep under tissue surface. Lowering illumination irradiance and increasing system sensitivity to detect weak fluorescence would offer a pathway to address these concerns. On this front, I demonstrated an endoscopic system that integrates a rigid endoscope with high transmission within NIR and visible spectra with a low noise CMOS image sensor featuring multiple read-outs to offer high dynamic range. Results from preliminary sensitivity tests, preclinical and clinical studies demonstrate enhanced sensitivity of the system that would make it conducive toward MIS implementing NIR fluorescence imaging while minimizing the risk of probe photobleaching.

Another challenge that could impede NIR fluorescence imaging in MIS that I have addressed in my research involves how the information which is captured by the endoscopic system is displayed to the surgeon. Most FGS systems utilize 2D displays to visualize NIR fluorescence images for image guided surgery. However, several features that are available with natural eyesight are lost when accessing the fluorescence images on then 2D displays. For instance, when using 2D displays, the perception of depth is limited to monocular depth cues, which can be less accurate and intuitive than binocular depth cues available in human visual system. It becomes more problematic within the context of minimally invasive surgeries where visual access to the surgical

site and haptic senses are limited due to the use of small incisions and specialized instruments which can make it more challenging to perform surgery. Using an intraoperative imaging system which incorporates the bioinspired image sensor and a holographic display, I demonstrated that is possible to overcome some of the limitations associated with 2D displays and provide surgeons with more accurate and natural perception of depth during surgical procedures. The results of several studies (chapter 5) from benchtop to *in vivo* animal studies demonstrate that the holographic goggles combined with the bioinspired imaging sensor improved accuracy and efficiency in identifying and removing tumors. The holographic display allows for real-time projection of fluorescence signals onto a see-through display, enabling the surgeon to access the surgical site through natural vision.

By tailoring surgical approaches to individual patient needs, personalized patient care can improve surgical outcomes. Every cancer patient has unique treatment needs, and there is no universal solution. My contribution mainly involves the development of two endoscopic systems, each with a unique feature set. The first one features multiple-fluorophore imaging to enhance the sensitivity and specificity of cancer detection while the latter detects a single tracer but exhibits high sensitivity. I also demonstrated the significance of displaying the fluorescence information with improved depth perception. In summary, having a combination of probes with high photostability, tumor targeting ability, and quantum yield characteristics with an endoscopic system which features high NIR fluorescence sensitivity and spectral sensitivity along with a display that enhances depth perception has the potential to revolutionize fluorescence imaging in minimally invasive surgeries. I am confident that my work offers solutions to meet several of these requirements and pave the way for the advancement of the field.

References

[1] Mebin B. George, Benjamin Lew, Steven Blair, Zhongmin Zhu, Zuodong Liang, Indrajit Srivastava, et al. Bioinspired color-near infrared endoscopic imaging system for molecular guided cancer surgery. J Biomed Opt 2023;28.

[2] Siegel RL, Miller KD, Fuchs HE, Jemal A. Cancer statistics, 2022. CA Cancer J Clin 2022;72. https://doi.org/10.3322/caac.21708.

[3] Sung H, Ferlay J, Siegel RL, Laversanne M, Soerjomataram I, Jemal A, et al. Global Cancer Statistics 2020: GLOBOCAN Estimates of Incidence and Mortality Worldwide for 36 Cancers in 185 Countries. CA Cancer J Clin 2021;71. https://doi.org/10.3322/caac.21660.

[4] Meric F, Mirza NQ, Vlastos G, Buchholz TA, Kuerer HM, Babiera G V., et al. Positive surgical margins and ipsilateral breast tumor recurrence predict disease-specific survival after breast-conserving therapy. Cancer 2003;97. https://doi.org/10.1002/cncr.11222.

[5] Snijder RJ, De La Rivière AB, Eibers HJJ, Van Den Bosch JMM. Survival in resected stage I lung cancer with residual tumor at the bronchial resection margin. Annals of Thoracic Surgery, vol. 65, 1998. https://doi.org/10.1016/S0003-4975(97)01114-4.

[6] Nagtegaal ID, Quirke P. What is the role for the circumferential margin in the modern treatment of rectal cancer? Journal of Clinical Oncology 2008;26. https://doi.org/10.1200/JCO.2007.12.7027.

[7] Singletary SE. Surgical margins in patients with early-stage breast cancer treated with breast conservation therapy. Am J Surg 2002;184. https://doi.org/10.1016/S0002-9610(02)01012-7.

[8] Sun J, Garfield DH, Lam B, Yan J, Gu A, Shen J, et al. The value of autofluorescence bronchoscopy combined with white light bronchoscopy compared with white light alone in the diagnosis of intraepithelial neoplasia and invasive lung cancer: A meta-analysis. Journal of Thoracic Oncology 2011;6. https://doi.org/10.1097/JTO.0b013e318220c984.

[9] Knight SB, Crosbie PA, Balata H, Chudziak J, Hussell T, Dive C. Progress and prospects of early detection in lung cancer. Open Biol 2017;7. https://doi.org/10.1098/rsob.170070.

[10] Handbook of Biomedical Fluorescence. 2003. https://doi.org/10.1201/9780203912096.

[11] Zhang J, Wu J, Yang Y, Liao H, Xu Z, Hamblin LT, et al. White light, autofluorescence and narrow-band imaging bronchoscopy for diagnosing airway pre-cancerous and early cancer lesions: A systematic review and meta-analysis. J Thorac Dis 2016;8. https://doi.org/10.21037/jtd.2016.11.61.

[12] Elahi SF, Wang TD. Future and advances in endoscopy. J Biophotonics 2011;4. https://doi.org/10.1002/jbio.201100048.

[13] Muguruma N, Miyamoto H, Okahisa T, Takayama T. Endoscopic molecular imaging: Status and future perspective. Clin Endosc 2013;46. https://doi.org/10.5946/ce.2013.46.6.603.

[14] Ali T, Choyke PL, Kobayashi H. Endoscopic molecular imaging of cancer. Future Oncology 2013;9. https://doi.org/10.2217/fon.13.123.

[15] Hirsch FR, Prindiville SA, Miller YE, Franklin WA, Dempsey EC, Murphy JR, et al. Fluorescence versus white-light bronchoscopy for detection of preneoplastic lesions: A randomized study. J Natl Cancer Inst 2001;93. https://doi.org/10.1093/jnci/93.18.1385.

[16] Rivera MP, Mehta AC, Wahidi MM. Establishing the diagnosis of lung cancer: Diagnosis and management of lung cancer, 3rd ed: American college of chest physicians evidence-based clinical practice guidelines. Chest 2013;143. https://doi.org/10.1378/chest.12-2353.

[17] Ozaki S, Ohara M. Endoscopy-assisted breast-conserving surgery for breast cancer patients. Gland Surg 2014;3.

[18] Prasad GA, Buttar NS, Wongkeesong LM, Lewis JT, Sanderson SO, Lutzke LS, et al. Significance of neoplastic involvement of margins obtained by endoscopic mucosal resection in Barrett's esophagus. American Journal of Gastroenterology 2007;102. https://doi.org/10.1111/j.1572-0241.2007.01419.x.

[19] Jafari A, Shen SA, Qualliotine JR, Orosco RK, Califano JA, DeConde AS. Impact of margin status on survival after surgery for sinonasal squamous cell carcinoma. Int Forum Allergy Rhinol 2019;9. https://doi.org/10.1002/alr.22415.

[20] Rhodes JM, Campbell BJ. Inflammation and colorectal cancer: IBD-associated and sporadic cancer compared. Trends Mol Med 2002;8. https://doi.org/10.1016/S1471-4914(01)02194-3.

[21] DSouza A V., Lin H, Henderson ER, Samkoe KS, Pogue BW. Review of fluorescence guided surgery systems: identification of key performance capabilities beyond indocyanine green imaging. J Biomed Opt 2016;21. https://doi.org/10.1117/1.jbo.21.8.080901.

[22] Mao Y, Wang K, He K, Ye J, Yang F, Zhou J, et al. Development and application of the near-infrared and white-light thoracoscope system for minimally invasive lung cancer surgery. J Biomed Opt 2017;22. https://doi.org/10.1117/1.jbo.22.6.066002.

[23] van Keulen S, Nishio N, Fakurnejad S, Birkeland A, Martin BA, Lu G, et al. The clinical application of fluorescence-guided surgery in head and neck cancer. Journal of Nuclear Medicine 2019;60. https://doi.org/10.2967/jnumed.118.222810.

[24] Hart ZP, Nishio N, Krishnan G, Lu G, Zhou Q, Fakurnejad S, et al. Endoscopic Fluorescence-Guided Surgery for Sinonasal Cancer Using an Antibody-Dye Conjugate. Laryngoscope 2020;130. https://doi.org/10.1002/lary.28483.

[25] Handgraaf HJM, Verbeek FPR, Tummers QRJG, Boogerd LSF, Van De Velde CJH, Vahrmeijer AL, et al. Real-time near-infrared fluorescence guided surgery in gynecologic oncology: A review of the current state of the art. Gynecol Oncol 2014;135. https://doi.org/10.1016/j.ygyno.2014.08.005.

[26] Baldus SE, Schaefer KL, Engers R, Hartleb D, Stoecklein NH, Gabbert HE. Prevalence and heterogeneity of KRAS, BRAF, and PIK3CA mutations in primary colorectal adenocarcinomas and their corresponding metastases. Clinical Cancer Research 2010;16. https://doi.org/10.1158/1078-0432.CCR-09-2446.

[27] Pogue BW. Perspective review of what is needed for molecular-specific fluorescence-guided surgery. J Biomed Opt 2018;23. https://doi.org/10.1117/1.jbo.23.10.100601.

[28] Fearon ER. Molecular genetics of colorectal cancer. Annual Review of Pathology: Mechanisms of Disease 2011;6. https://doi.org/10.1146/annurev-pathol-011110-130235.

[29] Miller SJ, Lee CM, Joshi BP, Gaustad A, Seibel EJ, Wang TD. Targeted detection of murine colonic dysplasia in vivo with flexible multispectral scanning fiber endoscopy. J Biomed Opt 2012;17. https://doi.org/10.1117/1.jbo.17.2.021103.

[30] Kijanka MM, van Brussel ASA, van der Wall E, Mali WPTM, van Diest PJ, van Bergen en Henegouwen PMP, et al. Optical imaging of pre-invasive breast cancer with a combination of VHHs targeting CAIX and HER2 increases contrast and facilitates tumour characterization. EJNMMI Res 2016;6. https://doi.org/10.1186/s13550-016-0166-y.

[31] Vahrmeijer AL, Hutteman M, Van Der Vorst JR, Van De Velde CJH, Frangioni J V. Image-guided cancer surgery using near-infrared fluorescence. Nat Rev Clin Oncol 2013;10. https://doi.org/10.1038/nrclinonc.2013.123.

[32] Samkoe KS, Tichauer KM, Gunn JR, Wells WA, Hasan T, Pogue BW. Quantitative in vivo immunohistochemistry of epidermal growth factor receptor using a receptor concentration imaging approach. Cancer Res 2014;74. https://doi.org/10.1158/0008-5472.CAN-14-0141.

[33] Bogdanova R, Boulanger P, Zheng B. Depth perception of surgeons in minimally invasive surgery. Surg Innov 2016;23. https://doi.org/10.1177/1553350616639141.

[34] Blair S, Garcia M, Davis T, Zhu Z, Liang Z, Konopka C, et al. Hexachromatic bioinspired camera for image-guided cancer surgery. Sci Transl Med 2021;13. https://doi.org/10.1126/scitranslmed.aaw7067.

[35] Etzioni R, Urban N, Ramsey S, McIntosh M, Schwartz S, Reid B, et al. The case for early detection. Nat Rev Cancer 2003;3. https://doi.org/10.1038/nrc1041.

[36] Randall LM, Wenham RM, Low PS, Dowdy SC, Tanyi JL. A phase II, multicenter, open-label trial of OTL38 injection for the intra-operative imaging of folate receptor-alpha positive ovarian cancer. Gynecol Oncol 2019;155. https://doi.org/10.1016/j.ygyno.2019.07.010.

[37] Mahalingam SM, Kularatne SA, Myers CH, Gagare P, Norshi M, Liu X, et al. Evaluation of Novel Tumor-Targeted Near-Infrared Probe for Fluorescence-Guided Surgery of Cancer. J Med Chem 2018;61. https://doi.org/10.1021/acs.jmedchem.8b01115.

[38] Glatz J, Varga J, Garcia-Allende PB, Koch M, Greten FR, Ntziachristos V. Concurrent video-rate color and near-infrared fluorescence laparoscopy. J Biomed Opt 2013;18. https://doi.org/10.1117/1.jbo.18.10.101302.

[39] Oh G, Cho HJ, Suh S, Ji Y, Chung HS, Lee D, et al. Multicolor fluorescence imaging using a single RGB-IR CMOS sensor for cancer detection with smURFP-labeled probiotics. Biomed Opt Express 2020;11. https://doi.org/10.1364/boe.391417.

[40] Garcia-Allende PB, Glatz J, Koch M, Tjalma JJ, Hartmans E, Terwisscha van Scheltinga AGT, et al. Towards clinically translatable NIR fluorescence molecular guidance for colonoscopy. Biomed Opt Express 2014;5. https://doi.org/10.1364/boe.5.000078.

[41] Suo Y, Wu F, Xu P, Shi H, Wang T, Liu H, et al. NIR-II Fluorescence Endoscopy for Targeted Imaging of Colorectal Cancer. Adv Healthc Mater 2019;8. https://doi.org/10.1002/adhm.201900974.

[42] Kulhari H, Pooja D, Shrivastava S, Telukutala SR, Barui AK, Patra CR, et al. Cyclic-RGDfK peptide conjugated succinoyl-TPGS nanomicelles for targeted delivery of docetaxel to integrin receptor over-expressing angiogenic tumours. Nanomedicine 2015;11. https://doi.org/10.1016/j.nano.2015.04.007.

[43] Schmitt A, Schmitt J, Münch G, Gasic-Milencovic J. Characterization of advanced glycation end products for biochemical studies: Side chain modifications and fluorescence characteristics. Anal Biochem 2005;338. https://doi.org/10.1016/j.ab.2004.12.003.

[44] Burley TA, Da Pieve C, Martins CD, Ciobota DM, Allott L, Oyen WJG, et al. Affibody-based PET imaging to guide EGFR-targeted cancer therapy in head and neck squamous cell cancer models. Journal of Nuclear Medicine 2019;60. https://doi.org/10.2967/jnumed.118.216069.

[45] Trapnell C, Williams BA, Pertea G, Mortazavi A, Kwan G, Van Baren MJ, et al. Transcript assembly and quantification by RNA-Seq reveals unannotated transcripts and isoform switching during cell differentiation. Nat Biotechnol 2010;28. https://doi.org/10.1038/nbt.1621.

[46] Roberts A, Trapnell C, Donaghey J, Rinn JL, Pachter L. Improving RNA-Seq expression estimates by correcting for fragment bias. Genome Biol 2011;12. https://doi.org/10.1186/gb-2011-12-3-r22.

[47] Roberts A, Pimentel H, Trapnell C, Pachter L. Identification of novel transcripts in annotated genomes using RNA-seq. Bioinformatics 2011;27. https://doi.org/10.1093/bioinformatics/btr355.

[48] Trapnell C, Hendrickson DG, Sauvageau M, Goff L, Rinn JL, Pachter L. Differential analysis of gene regulation at transcript resolution with RNA-seq. Nat Biotechnol 2013;31. https://doi.org/10.1038/nbt.2450.

[49] Suurs F V., Qiu SQ, Yim JJ, Schröder CP, Timmer-Bosscha H, Bensen ES, et al. Fluorescent image-guided surgery in breast cancer by intravenous application of a quenched fluorescence activity-based probe for cysteine cathepsins in a syngeneic mouse model. EJNMMI Res 2020;10. https://doi.org/10.1186/s13550-020-00688-0.

[50] Puangmali P, Althoefer K, Seneviratne LD, Murphy D, Dasgupta P. State-of-the-art in force and tactile sensing for minimally invasive surgery. IEEE Sens J 2008;8. https://doi.org/10.1109/JSEN.2008.917481.

[51] Demi B, Ortmaier T, Seibold U. The touch and feel in minimally invasive surgery. HAVE 2005: IEEE International Workshop on Haptic Audio Visual Environments and their Applications, vol. 2005, 2005. https://doi.org/10.1109/HAVE.2005.1545648.

[52] Li Y, Zhu Z, Chen JJ, Jing JC, Sun C-H, Kim S, et al. Multimodal endoscopy for colorectal cancer detection by optical coherence tomography and near-infrared fluorescence imaging. Biomed Opt Express 2019;10. https://doi.org/10.1364/boe.10.002419.

[53] Yoon SM, Myung SJ, Kim IW, Do EJ, Ye BD, Ryu JH, et al. Application of near-infrared fluorescence imaging using a polymeric nanoparticle-based probe for the diagnosis and therapeutic monitoring of colon cancer. Dig Dis Sci 2011;56. https://doi.org/10.1007/s10620-011-1685-z.

[54] Goetz M, Wang TD. Molecular Imaging in Gastrointestinal Endoscopy. Gastroenterology 2010;138. https://doi.org/10.1053/j.gastro.2010.01.009.

[55] Coda S, Siersema P, Stamp G, Thillainayagam A. Biophotonic endoscopy: a review of clinical research techniques for optical imaging and sensing of early gastrointestinal cancer. Endosc Int Open 2015;03. https://doi.org/10.1055/s-0034-1392513.

[56] Keating JJ, Runge JJ, Singhal S, Nims S, Venegas O, Durham AC, et al. Intraoperative near-infrared fluorescence imaging targeting folate receptors identifies lung cancer in a large-animal model. Cancer 2017;123. https://doi.org/10.1002/cncr.30419.

[57] Kosaka N, Mitsunaga M, Longmire MR, Choyke PL, Kobayashi H. Near infrared fluorescence-guided real-time endoscopic detection of peritoneal ovarian cancer nodules using intravenously injected indocyanine green. Int J Cancer 2011;129. https://doi.org/10.1002/ijc.26113.

[58] Newton AD, Predina JD, Corbett CJ, Frenzel-Sulyok LG, Xia L, Petersson EJ, et al. Optimization of Second Window Indocyanine Green for Intraoperative Near-Infrared Imaging of Thoracic Malignancy. J Am Coll Surg 2019;228. https://doi.org/10.1016/j.jamcollsurg.2018.11.003.

[59] Low PS, Singhal S, Srinivasarao M. Fluorescence-guided surgery of cancer: applications, tools and perspectives. Curr Opin Chem Biol 2018;45. https://doi.org/10.1016/j.cbpa.2018.03.002.

[60] Van Keulen S, Hom M, White · Haley, Rosenthal EL, Baik FM. The Evolution of Fluorescence-Guided Surgery. Mol Imaging Biol n.d. https://doi.org/10.1007/s11307-022-01772-8.

[61] Fiorelli A, Carlucci A, Natale G, Bove M, Freda C, Noro A, et al. Survival after video-assisted thoracoscopic surgery for lung metastasectomy. Video Assist Thorac Surg 2021;6. https://doi.org/10.21037/vats-2020-lm-02.

[62] Andolfi M, Potenza R, Capozzi R, Liparulo V, Puma F, Yasufuku K. The role of bronchoscopy in the diagnosis of early lung cancer: A review. J Thorac Dis 2016;8. https://doi.org/10.21037/jtd.2016.11.81.

[63] Haruki T, Miwa K, Araki K, Taniguchi Y, Nakamura H. Distribution and Prevalence of Locoregional Recurrence after Video-Assisted Thoracoscopic Surgery for Primary Lung

Cancer. Thoracic and Cardiovascular Surgeon 2016;64. https://doi.org/10.1055/s-0035-1550231.

[64] Blair S, Deliwala A, Chen E, Subashbabu S, Li A, George M, et al. A 3.47 e- Read noise, 81 dB dynamic range backside-illuminated multispectral imager for near-infrared fluorescence image-guided surgery. Proceedings - IEEE International Symposium on Circuits and Systems, vol. 2020- October, 2020. https://doi.org/10.1109/iscas45731.2020.9180737.

[65] van Manen L, Handgraaf HJM, Diana M, Dijkstra J, Ishizawa T, Vahrmeijer AL, et al. A practical guide for the use of indocyanine green and methylene blue in fluorescence-guided abdominal surgery. J Surg Oncol 2018;118. https://doi.org/10.1002/jso.25105.

[66] Hernot S, van Manen L, Debie P, Mieog JSD, Vahrmeijer AL. Latest developments in molecular tracers for fluorescence image-guided cancer surgery. Lancet Oncol 2019;20. https://doi.org/10.1016/S1470-2045(19)30317-1.

[67] Zhang RR, Schroeder AB, Grudzinski JJ, Rosenthal EL, Warram JM, Pinchuk AN, et al. Beyond the margins: Real-time detection of cancer using targeted fluorophores. Nat Rev Clin Oncol 2017;14. https://doi.org/10.1038/nrclinonc.2016.212.

[68] Wang S, Liu X, Zhou P. The Road for 2D Semiconductors in the Silicon Age. Advanced Materials 2022;34. https://doi.org/10.1002/adma.202106886.

[69] Heiskanen V, Hamblin MR. Photobiomodulation: Lasers: vs. light emitting diodes? Photochemical and Photobiological Sciences 2018;17. https://doi.org/10.1039/c8pp00176f.

[70] Shao P, Ding H, Wang J, Liu P, Ling Q, Chen J, et al. Designing a Wearable Navigation System for Image-Guided Cancer Resection Surgery. Ann Biomed Eng 2014;42. https://doi.org/10.1007/s10439-014-1062-0.

[71] Liu Y, Njuguna R, Matthews T, Akers WJ, Sudlow GP, Mondal S, et al. Near-infrared fluorescence goggle system with complementary metal–oxide–semiconductor imaging sensor and see-through display. J Biomed Opt 2013;18. https://doi.org/10.1117/1.jbo.18.10.101303.

[72] Mondal SB, Gao S, Zhu N, Liang R, Gruev V, Achilefu S. Real-time fluorescence image-guided oncologic surgery. Adv Cancer Res, vol. 124, 2014. https://doi.org/10.1016/B978-0-12-411638-2.00005-7.

[73] Kolodzey L, Grantcharov PD, Rivas H, Schijven MP, Grantcharov TP. Wearable technology in the operating room: A systematic review. BMJ Innov 2017;3. https://doi.org/10.1136/bmjinnov-2016-000133.

[74] Suzuki S, be KA. Topological structural analysis of digitized binary images by border following. Comput Vis Graph Image Process 1985;30. https://doi.org/10.1016/0734-189X(85)90016-7.

[75] Cui N, Kharel P, Gruev V. Augmented reality with Microsoft HoloLens holograms for near infrared fluorescence based image guided surgery. Molecular-Guided Surgery: Molecules, Devices, and Applications III, vol. 10049, 2017. https://doi.org/10.1117/12.2251625.

[76] Antoniou SA, Antoniou GA, Antoniou AI, Granderath FA. Past, present, and future of minimally invasive abdominal surgery. Journal of the Society of Laparoendoscopic Surgeons 2015;19. https://doi.org/10.4293/JSLS.2015.00052.

[77] Kumar A, Yadav N, Singh S, Chauhan N. Minimally invasive (endoscopic-computer assisted) surgery: Technique and review. Ann Maxillofac Surg 2016;6. https://doi.org/10.4103/2231-0746.200348.

[78] Debie P, Hernot S. Emerging fluorescent molecular tracers to guide intra-operative surgical decision-making. Front Pharmacol 2019;10. https://doi.org/10.3389/fphar.2019.00510.

[79] Barth CW, Gibbs S. Fluorescence image-guided surgery: a perspective on contrast agent development, 2020. https://doi.org/10.1117/12.2545292.

[80] Miller SE, Tummers WS, Teraphongphom N, van den Berg NS, Hasan A, Ertsey RD, et al. First-in-human intraoperative near-infrared fluorescence imaging of glioblastoma using cetuximab-IRDye800. J Neurooncol 2018;139. https://doi.org/10.1007/s11060-018-2854-0.

[81] Gong L, Ding H, Long NE, Sullivan BJ, Martin EW, Magliery TJ, et al. A 3E8.scFv.Cys-IR800 Conjugate Targeting TAG-72 in an Orthotopic Colorectal Cancer Model. Mol Imaging Biol 2018;20. https://doi.org/10.1007/s11307-017-1096-4.

[82] O'Shannessy DJ, Yu G, Smale R, Fu YS, Singhal S, Thiel RP, et al. Folate receptor alpha expression in lung cancer: Diagnostic and prognostic significance. Oncotarget 2012;3. https://doi.org/10.18632/oncotarget.519.

[83] Nunez MI, Behrens C, Woods DM, Lin H, Suraokar M, Kadara H, et al. High expression of folate receptor alpha in lung cancer correlates with adenocarcinoma histology and mutation. Journal of Thoracic Oncology 2012;7. https://doi.org/10.1097/JTO.0b013e31824de09c.

[84] Shi H, Guo J, Li C, Wang Z. A current review of folate receptor alpha as apotential tumor target in non-small-cell lung cancer. Drug Des Devel Ther 2015;9. https://doi.org/10.2147/DDDT.S90670.